Received 20 December 2023; revised 30 January 2024; accepted 11 March 2024. Date of publication 18 March 2024; date of current version 4 April 2024.

Digital Object Identifier 10.1109/OJCOMS.2024.3377720

Hardware-Aware Joint Localization-Synchronization and Tracking Using Reconfigurable Intelligent Surfaces in 5G and Beyond

DEEB ASSAD TUBAIL [1] (Graduate Student Member, IEEE), MOHAMMED EL-ABSI [2] (Member, IEEE), SALAMA IKKI [1] (Senior Member, IEEE), AND THOMAS KAISER [2] (Senior Member, IEEE)

[1]Electrical and Computer Engineering Department, Lakehead University, Thunder Bay, ON P7B 5E1, Canada

[2]Institute of Digital Signal Processing, Duisburg-Essen University, 47057 Duisburg, Germany

CORRESPONDING AUTHOR: D. TUBAIL (e-mail: dtubail@lakeheadu.ca)

This work was supported by the Deutsche Forschungsgemeinschaft (DFG, German Research Foundation) through Project S04 under Project 287022738 TRR 196.

ABSTRACT This work investigates joint localization-synchronization and tracking in 5G and beyond. In particular, we target realistic circumstances where the theoretical assumptions of a perfect synchronous system and ideal transceivers no longer exist. We take a close look at the multiple-input single-output (MISO) millimeter-wave (*mm*wave) system that employs the orthogonal frequency-division multiplexing (OFDM), with the existence of the reconfigurable intelligent surface (RIS). Given the known positions of the RIS and the base station (BS), the single antenna mobile station (MS) can estimate its position and jointly synchronize itself with the multiple antennas BS. This can be accomplished using a maximum likelihood estimator (MLE) whose cost function accounts for the transceivers' hardware impairments (HWIs). In our tracking scenario, the Kalman filter based tracker (KFT) follows the MLE by paying attention to HWIs-driven accuracy degradation. We then present the theoretical bounds of the tracking accuracy, expressed in terms of the Bayesian Cramer-Rao bound (BCRB). Finally, we conduct computer simulations to demonstrate the adverse deterioration in the joint localization-synchronization process accuracy as well as the accuracy of tracking due to the HWIs.

INDEX TERMS Estimation, localization, tracking, synchronization, hardware impairments, RIS, millimeter, fisher information matrix.

I. INTRODUCTION

RADIO localization and tracking have seen significant growth in the fifth generation (5G) of cellular systems and are not limited to emergencies anymore. Significantly, with millimeter-wave (*mm*wave) techniques, high-precision estimation, localization and tracking are anticipated due to the unprecedented bandwidth these systems offer. This is further enhanced by the deployment of antenna array technologies [1], [2], [3]. Consequently, the estimation, localization and tracking processes with *mm*wave technologies have been extensively studied in [1], [2], [3], [4], [5], [6], [7]. In particular, the theoretical performance bounds for the orientation and the positioning in the *mm*wave systems were calculated in terms of Cramer-Rao bound (CRB) in [1], [2], [3]. Moreover, [4] provided estimations for the angle-of-arrival (AoA) and angle-of-departure (AoD) in *mm*wave channels, while [5] and [6] investigated the localization problem. The work in [7] addressed tracking the slow variations of AoDs and AoAs, as well as detecting abrupt changes in a mobile user's movements.

More interestingly, deploying reconfigurable intelligent surface (RIS) technology addresses challenging issues in radio localization and tracking. For instance, the multiple paths created by the RISs, facilitate the estimation of AoD, AoA and time of arrival (ToA). Moreover, the RIS technique enables the joint localization-synchronization process,

especially in single-input single-output (SISO) systems [8]. RIS also enhances estimation performance, benefiting localization and tracking. To this end, the literature in [9] addressed the escalating need for precise positioning by exploring RIS technology. The study delves into the evolving research and development of RIS, outlining localization principles and highlighting its potential in positioning. A thorough survey of current RIS-assisted localization research is provided, concluding with a discussion on key challenges that warrant attention in future research endeavours. In this context, the localization process in the presence of RIS has been addressed in [10], [11], [12], [13]. The position error bound (PEB) and the orientation error bound (OEB) were derived in [10] for a 2D RIS-aided *mm*wave localization process. Additionally, the work in [11] examined the impact of the number of RIS elements and the phase shifters values on the position estimation accuracy. This paper also presented the role of the RIS in improving localization accuracy by comparing it with the conventional system that includes one line-of-sight (LoS) and one non-LoS (NLoS). Moreover, the study conducted in [14] established the fundamental constraints on localizing a stationary MS in OFDM RIS-aided systems. Additionally, the study referenced in [15] derived the Bayesian analysis when estimating the location and orientation of the RIS in RIS-aided systems, or when the position and orientation offsets of the RISs become parameters that need to be estimated and fed back to the BS for correction. Both works made the assumption of perfect synchronization and ideal transceivers. Furthermore, the works in [12] and [13] executed the joint localization-synchronization process, comparing the attained accuracy against the CRB benchmark for evaluation.

In the context of tracking processes in RIS-assisted systems, studies [16], [17], [18], [19], [20] explored the tracking process in systems employing both RIS and multiple-input multiple-output (MIMO) technology, besides proposing algorithms for tracking time-varying channels and mobile terminals. Additionally, in [19], the Bayesian Cramer-Rao bound (BCRB) was derived as a theoretical mean square error (MSE) lower bound of the considered tracking problem. Furthermore, the study in [20] explored using RIS in vehicle platoons, working alongside a BS to enhance high-precision location tracking. The RIS introduces structured sparsity, aligning with the initial sparse LoS channels of the BS, leading to beneficial group sparsity. This group sparsity boosts the energies of the original direct-only channel, concentrating the LoS channel energies from the same vehicle location index.

It is noteworthy that all the previously mentioned works assumed the localization and tracking processes were performed by ideal transceivers. This unrealistic assumption obscures the true accuracy of the mentioned processes, as hardware impairments (HWIs) invariably compromise performance [21], [22]. The deployment and operation of different types of circuitry operating, especially at high frequencies such as in *mm*wave communications, is often severely limited by non-ideal hardware behaviour [23], [24]. The authors of [24], [25], [26] derived the CRB benchmark for localization in *mm*wave MIMO, *mm*wave multiple-input single-output (MISO) and RIS-aided *mm*wave SISO systems, demonstrating the harmful impacts of the HWIs on the localization in these systems. Subsequently, the authors of [25], [26] carried out a 3D localization process accounting for the HWIs and compared the accomplished accuracy with the CRB benchmark. Besides, the work in [27] designed custom auxiliary beams and pilots with the purpose of angle tracking in *mm*wave systems considering the array calibration errors, where the offline calibration is performed in advance to mitigate the impact of the array calibration errors on the tracking process. Moreover, a robust Bayesian tracker for AoA in *mm*wave MIMO systems is presented in [28]. This work tackled uncertainty stemming from the restricted resolution of the phase shifters, modeling this uncertainty as a discrete Gaussian random variable with variance related to the degree of uncertainty. In [29], the phase noise error and channel gains parameters in *mm*wave MIMO system were tracked.

While the works in [27], [28], [29] investigated a particular HWIs source and its impact on the transition model of the tracked parameters, they overlooked the impacts of that specific HWIs source, as well as other HWIs sources, on the transmitted and received pilots. In practice, the HWIs severely harm the estimation, localization and tracking process, where the works in [25], [30], [31] presented the influence of different HWIs sources on the accuracy of these processes. Pertinently, [31] considered the impact of the HWIs on the measurements and the estimation process. Specifically, it derived BCRB and implemented the Kalman filter (KF) to track the range and the direction of mobile station (MS) relative to a reference base station (BS). Additionally, the work enhanced the tracking accuracy by providing an accurate description of the measurements degraded by HWIs, employing Monte Carlo (MC) techniques for this purpose.

Nonetheless, the studies in [24], [25], [26], [27], [28], [29], [30], [31] made another idealistic assumption: the perfect synchronization of the MS and BS prior to localization. On this matter, the works in [32] and [33] analyzed the localization process theoretically in terms of CRB without actually executing the localization process, considering both HWIs and imperfect synchronization. Specifically, the work in [32] considered the localization process in *mm*wave MIMO system when the synchronization was performed as a preliminary step before the localization. The work in [33] considered the case of performing the synchronization jointly with the localization in an RIS-aided *mm*wave system. Regrettably, both works confirmed that the perfect synchronization assumption covers up an unseen part of the degradation in the localization accuracy.

Motivated by these gaps in the existing literature, this work investigates the localization and tracking processes in 5G and beyond systems considering neither perfect synchronization

nor ideal hardware. Specifically, this work performs the joint localization-synchronization process and tracking in an asynchronous RIS-aided *mm*wave MISO-OFDM system experiencing HWIs.

A. RELATED-WORKS COMPARISON AND CONTRIBUTIONS

To the best of our knowledge, this study is the first to undertake the localization and tracking process for a mobile terminal within an asynchronous, hardware-impaired 3D RIS-aided *mm*wave MISO-OFDM system. Specifically, this work performs the joint localization-synchronization based on the maximum likelihood estimator (MLE) and executes the tracking via the KF. For evaluation, this work compares the joint localization-synchronization accuracy with CRB derived in [33] and derives the recursive BCRB to evaluate the tracking process.

In contrast to [1], [2], [3], [4], [5], [6], [7], [8], [10], [11], [12], [13], [16], [17], [18], [19], [20], this work addresses the practical case where the system is imperfect and equipped with hardware-impaired transceivers. This practical consideration is widely recognized to pose challenges and introduce new difficulties in tasks such as estimation, localization, tracking, and various other applications and processes. Besides, different from the works in [1], [2], [3], [4], [5], [6], [7], [10], [11], [16], [17], [18], [19], [20], [26], [30], [25], [27], [28], [29], [31], this work considers another tangible source of localization and tracking errors by presuming the system is not perfectly synchronized. Consequently, synchronizing the system either simultaneously with or before the localization and tracking processes becomes imperative. Implementing a joint localization-synchronization process necessitates the estimation of both LoS and NLoS parameters, which becomes increasingly challenging in the presence of HWIs. Furthermore, unlike the literature in [1], [2], [3], [4], [5], [6], [7], [8], [10], [11], [12], [13], [14], [15], [24], [25], [26], [32], [33] that addressed the case of a stationary MS, the current investigation considers the case of maneuvering MS besides the case of stationary MS. Maneuvering MS assumption transforms the localization process into a time-varying tracking process and converts the associated BCRB into a recursive benchmark. Additionally, this work counts the impact of the HWIs on the measurements, which was not considered in [27], [28], [29].

A detailed comparison with the most relevant literature is here. In terms of novelty, our study stands out as the first to leverage both the LoS and NLoS links (the latter bouncing off the RIS). This approach facilitates the joint execution of the localization and synchronization, while also factoring in synchronization errors on localization and tracking accuracy. Specifically, our previous work in [26] investigated the localization process in an RIS-aided *mm*wave system suffering from HWIs. Besides, the previous work in [26] considered the localization process and the associated benchmark only for the fixed position scenario, neglecting the examination of non-stationary MS's tracking process and benchmark derivation. Moreover, it did not capitalize on the LoS link for either localization or synchronization. Instead, it made the simplifying assumption of a system being perfectly synchronized prior to the initiation of the localization process. Moreover, although the LoS provides the most useful information for localization, the approach in [26] relied solely on parameters estimated from the NLoS link via the RIS, disregarding those originating from the LoS.

Moreover, the present study distinguishes itself from the literature cited [24], [25], [26], [32], [33] that delved into the processes of localization while considering HWIs. Notably, these previous works did not provide any solutions to improve localization accuracy or mitigate the influence of HWIs. It is important to highlight that achieving accurate positioning, which is affected by HWIs, synchronization errors, and maneuvering behaviour, especially when disregarding LoS parameters, necessitates additional processing and techniques.

Moreover, unlike the works in [33] and [32], our current work actualizes the localization and synchronization processes. Compared to [31], the tracking process explored differs from our current problem. Specifically, [31] focused on tracking the MS's range and direction relative to the reference BS based on the estimation of time of flight (ToF) and AoDs. In contrast, our method traces the MS's position using estimates derived from position. Needless to say, the results in [31] neglected the impact of synchronization error on tracking accuracy by assuming an unrealistically perfect synchronization between the BS and MS.

Consequently, the principal contributions of this study are succinctly presented in Table (1) and elaborated as follows:

- This study undertakes the localization process while taking into account two practical scenarios: HWIs and imperfect synchronization within the system. Following this, we deploy a joint localization-synchronization process that incorporates the influence of HWIs.
- This work suppresses the destructive impact of the HWIs on the joint localization-synchronization process accuracy. Initially, the approach involves processing the estimated position and clock offset by KF. Besides, it proposes utilizing the MC approach with KF for purposes of extra enhancement in accuracy.
- This work addresses mobile terminal tracking. Initially, we implement joint localization-synchronization for the mobile terminal at a given sample based on the MLE and its generalized cost function. The outcome of this initial step then feeds into the Kalman filter based tracker (KFT) that accounts for the accuracy of the localization process under the effects of HWIs, besides the state transition model of the mobile terminal. Also, here with the tracking process, MC approach with KFT is proposed for more improvement in the tracking accuracy.

TABLE 1. Summary of the new design/analytical challenges and contributions that were not addressed in the literature.

New challenges and differences	Contribution
Maneuvering terminal: introduces time-variant problem and benchmark.	• Detailing tracker based on KF subsequent to the joint localization-synchronization process. • Providing recursive BCRB benchmark.
Asynchronous system requires synchronization process besides the localization process considering the HWIs.	• Performing joint localization-synchronization process considering the HWIs. • Improving accuracy by leveraging pertinent CRB benchmark besides solutions based on KF.
Performing the joint localization-synchronization proces considering the HWIs.	• Estimating both the LoS and NLoS parameters that become challenging due to the presence of the HWIs.
Accuracy enhancement by mitigating the HWIs and synchronization errors	• Processing the joint localization-synchronization process outputs by implementing KF. • Implementing MC approach with KF instead of CRB to enhance the accuracy, since MC achieves a more realistic description of the joint localization-synchronization accuracy than CRB.

- We derive the Bayesian Fisher information matrix (BFIM), which is recursively calculated by combining the FIM from observed data with the priori information about the state transition model of the mobile terminal. Following this, we implement the inverse operation of the BFIM, which results in the BCRB benchmark. Subsequently, this benchmark facilitates the evaluation of the accuracy of the tracking process in a RIS-aided *mm*wave MISO-OFDM system influenced by the HWIs.

The remainder of this paper is organized as follows. Section II describes the localization system and the channel model, while Section III depicts the hardware impairments and the signaling models. Next, Section IV investigates the joint localization-synchronization process and tracking, while Section V derives the BCRB benchmark. Following that, Section VI presents the simulation results, and our conclusions are presented in Section VII.

Notations: We denote scalars with lowercase letters and present the vectors and matrices with boldface lowercase letters, and Boldface uppercase letters respectively. Besides, tr($\mathbf{A}$) and $|\mathbf{A}|$ are the trace and the determinant of the matrix $\mathbf{A}$, respectively. Moreover, $\mathbf{A} = \text{diag}(\mathbf{b})$ means that $\mathbf{A}$ is a diagonal matix with the vector $\mathbf{b}$ as the main diagonal. Furthermore, $(\cdot)^T$ and $(\cdot)^H$ are the transpose and the Hermitian operators, respectively, while $[\mathbf{A}]_{(i,j)}$ indicates to the element located in matrix $\mathbf{A}$ in the j^{th} column and the i^{th} row. Next, the expected value is presented by $\mathbb{E}\{\cdot\}$, and the complex Gaussian random variable with μ mean and σ^2 variance is referred by $\mathcal{CN}(\mu, \sigma^2)$.

II. SYSTEM DESCRIPTION AND CHANNEL MODEL

This section describes the 3D RIS-aided *mm*wave MISO-OFDM system and the associated *mm*wave channel, in which joint localization-synchronization and tracking are executed. Our focus in this work is on the impact of HWIs within the RIS-aided *mm*wave MISO-OFDM framework. Consequently, as we delve into the joint localization-synchronization and tracking, our analysis remains aligned with the system and channel models referenced in the literature, such as [13] and [12], where HWIs were not factored in, and [33], which takes HWIs into account.

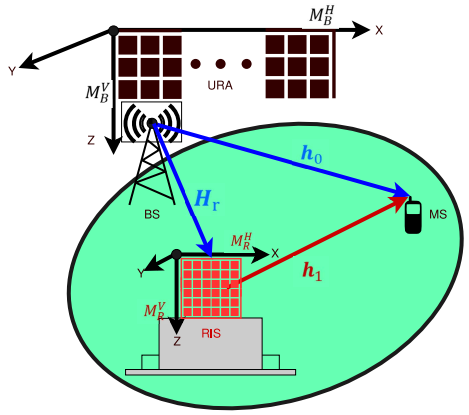

FIGURE 1. The RIS-aided *mm*wave MISO-OFDM system.

A. SYSTEM DESCRIPTION

Consider a single antenna MS, in an arbitrary time sample, occupying an unknown 3D position in the RIS-aided *mm*wave MISO-OFDM wireless communication system, as Fig. 1 illustrates. The MS receives directly from the BS equipped with M_{B} uniform rectangular arrays (URA), which have M_{B}^{H} horizontal antennas, M_{B}^{V} vertical antennas and thus $M_{\text{B}} = M_{\text{B}}^{\text{H}} \times M_{\text{B}}^{\text{V}}$ antennas in total. Simultaneously, the MS has an indirect link with the BS through an RIS equipped with M_{R} URA elements, which similarly has M_{R}^{H} horizontal elements, M_{R}^{V} vertical elements and thus $M_{\text{R}} = M_{\text{R}}^{\text{H}} \times M_{\text{R}}^{\text{V}}$ elements in total. Moreover, the system operates at f_c carrier frequency with bandwidth B that achieves the typical narrowband condition, i.e., $\lambda_n = c/(\frac{n}{NT} + f_c) \approx \lambda_c = c/f_c$ for $\forall n \in \{1, 2, \ldots, N\}$, where n is the subcarrier index, N is the subcarriers number, and $T = 1/B$ is the sampling period, while λ_c denotes the wavelength, and c is the speed of light.

B. CHANNEL MODEL

The complex channel vector of the direct link of the n^{th} subcarrier, $\mathbf{h}_0[n] \in \mathbb{C}^{M_{\text{B}} \times 1}$, can be defined as

$$\mathbf{h}_0[n] = \gamma_0 \alpha(\theta_0, \psi_0, M_{\text{B}}) \exp\left(-j2\pi n \tfrac{\tau_0}{NT}\right), \tag{1}$$

where the subscript "0" refers to the direct link between the MS and the BS and τ_0 is the signal propagation delay over the LoS link from the BS to the MS, which includes the clocks offset Δ, while ρ_0 and ϕ_0 are the magnitude and the phase of the complex amplitude of the LoS channel $\gamma_0 = \rho_0 e^{j\phi_0}$, respectively.

Following that, $\alpha(\theta_0, \psi_0, M_\mathrm{B}) \in \mathbb{C}^{M_\mathrm{B}\times 1}$ denotes the BS array steering vector associated with the LoS path. Generally, the steering vector α is a function of the number of antennas M, the azimuth AoD θ, and the elevation AoD ψ, where α is given by

$$\alpha(\theta, \psi, M) \in \mathbb{C}^{M\times 1} = \left[e^{j\frac{2\pi}{\lambda_c}\mathbf{k}(\theta,\psi)^\mathrm{T}u_1}, \ldots, e^{j\frac{2\pi}{\lambda_c}\mathbf{k}(\theta,\psi)^\mathrm{T}u_M}\right]^\mathrm{T}. \tag{2}$$

Here, $\mathbf{k}(\theta, \psi)$ is the wave vector that is defined as

$$\mathbf{k}(\theta, \psi) = [\sin\psi\cos\theta,\ \sin\psi\sin\theta,\ \cos\psi]^\mathrm{T}. \tag{3}$$

Besides, $\mathbf{u}_m$ is the location vector of the m^{th} antenna of the M URA, which can be given by

$$\mathbf{u}_m = \left[\mathrm{mod}\left(m-1, M^\mathrm{H}\right) \times d_\mathrm{H}\lambda_c, 0, \left\lfloor \frac{m-1}{M^\mathrm{H}} \right\rfloor \times d_\mathrm{V}\lambda_c\right]^\mathrm{T}, \tag{4}$$

where $d_\mathrm{H}\lambda_c$ and $d_\mathrm{V}\lambda_c$ stand for the horizontal and vertical inter-element spacing, respectively.

Next, as shown in Fig. 1, the RIS creates an NLoS path between the BS and MS, in which the incident signal on the RIS from the transmitter over $\mathbf{H}_\mathrm{r}[n] \in \mathbb{C}^{M_\mathrm{B}\times M_\mathrm{R}}$ link is beamed to the MS over $\mathbf{h}_1[n] \in \mathbb{C}^{M_\mathrm{R}\times 1}$ path. Here, the BS-RIS path over the n^{th} subcarrier is

$$\mathbf{H}_\mathrm{r}[n] = \gamma_\mathrm{r}\alpha(\theta_\mathrm{r}, \psi_\mathrm{r}, M_\mathrm{B})\left(\alpha(\bar{\theta}_\mathrm{r}, \bar{\psi}_\mathrm{r}, M_\mathrm{R})\right)^\mathrm{T} e^{\left(-j2\pi n\frac{\tau_\mathrm{r}}{NT}\right)}, \tag{5}$$

where the subscript "r" refers to the link between the BS and the RIS, $\gamma_\mathrm{r} = \rho_\mathrm{r} e^{j\phi_\mathrm{r}}$ is the complex amplitude of the BS-RIS link, and τ_r is the propagation time for the same link. By defining θ_r and ψ_r as the azimuth and elevation AoD from the BS, the BS steering vector is $\alpha(\theta_\mathrm{r}, \psi_\mathrm{r}, M_\mathrm{B}) \in \mathbb{C}^{M_\mathrm{B}\times 1}$ and is given according to (2). In the same context, as $\bar{\theta}_\mathrm{r}$ and $\bar{\psi}_\mathrm{r}$ are the azimuth and elevation AoA to the RIS, the associated steering vector is $\alpha(\bar{\theta}_\mathrm{r}, \bar{\psi}_\mathrm{r}, M_\mathrm{R}) \in \mathbb{C}^{M_\mathrm{R}\times 1}$ and also is calculated from (2). Besides, the wave vectors $\mathbf{k}(\theta_\mathrm{r}, \psi_\mathrm{r})$ and $\mathbf{k}(\bar{\theta}_\mathrm{r}, \bar{\psi}_\mathrm{r})$ are defined according to (3), where the RIS's elements interspace is d_r.

Coming to the RIS-MS link associated with the n^{th} subcarrier, $\mathbf{h}_1[n] \in \mathbb{C}^{M_\mathrm{R}\times 1}$, it can be given as

$$\mathbf{h}_1[n] = \gamma_1\alpha(\theta_1, \psi_1, M_\mathrm{R})\exp\left(-j2\pi n\frac{\tau_1}{NT}\right), \tag{6}$$

where the subscript "1" refers to the link between them RIS and MS, τ_1 is the RIS-MS link propagation delay including Δ, $\gamma_1 = \rho_1 e^{j\phi_1}$ is the complex gain over the RIS-MS link, and $\alpha(\theta_1, \psi_1, M_\mathrm{R}) \in \mathbb{C}^{M_\mathrm{R}\times 1}$ is the array steering vector.

Accordingly, the BS-MS NLoS link through the RIS, $\mathbf{h}^g_{\mathrm{NLoS}}[n] \in \mathbb{C}^{M_\mathrm{B}\times 1}$, is given by

$$\mathbf{h}^g_{\mathrm{NLoS}}[n] = \mathbf{H}_\mathrm{r}[n]\Omega^g\mathbf{h}_1[n], \tag{7}$$

where Ω^g is the phase control matrix of the RIS at transmission g, which is a diagonal matrix with unit-modulus entries, i.e., $\Omega^g \in \mathbb{C}^{M_\mathrm{R}\times M_\mathrm{R}} = \mathrm{diag}([e^{j\omega^g_1}, \ldots, e^{j\omega^g_{M_\mathrm{R}}}])$.

Consequently, the BS-MS channel including the LoS and the NLoS paths considering the n^{th} subcarrier and the g^{th} transmission is

$$\mathbf{h}^g[n] \in \mathbb{C}^{M_\mathrm{B}\times 1} = \mathbf{h}_0[n] + \mathbf{H}_\mathrm{r}[n]\Omega^g\mathbf{h}_1[n]. \tag{8}$$

It is worth noting in this work, NLoS components reflected over unknown position scatterers are neglected. This is because they suffer from high attenuation in *mm*wave, and thus, can be easily isolated based on the received power due to path orthogonality [3], [13], [26], [30], [34]. Nonetheless, for more details, the work in [25] presents the NLoS components in the system and their impact on the estimation process.

III. HARDWARE IMPAIRMENT AND SIGNAL MODELS

It is easy to recognize in practice, hardware components exhibit non-linear behaviors, which are referred to as HWIs. These include power amplifier non-linearity, amplitude/phase imbalance in I/Q mixers, phase noise in LoS, sampling jitter, and finite-resolution quantization in analog-to-digital converters, as covered in [21], [35], [36], [37] and references therein. To address this, analog or digital compensation algorithms have been proposed to mitigate the deterioration in hardware efficiency. Unfortunately, in all practical scenarios, these algorithms cannot completely remove the HWIs, resulting in a residual amount of these impairments that still causes significant performance degradation. This residual is referred to as *residual* HWIs [21].

This work aims at investigating the impact of HWIs on estimation, and consequently, on localization and tracking performance, regardless of the source of the HWIs. Therefore, this work will not delve into the detailed modeling, but will focus on a general model described in [38] and [21], which reflects the non-linear behaviors of the residual HWIs. This model has been frequently utilized in works that considered general HWIs, non-specific to one type of HWIs, as seen in [21], [24], [25], [26], [30], [32], [38].

A. HARDWARE IMPAIRMENTS MODEL

Fig. 2 illustrates the modeling of residual HWIs as a nonlinear memoryless function, which is described as [21]:

$$y = \sqrt{\kappa}x + \eta, \tag{9}$$

where $x \sim \mathcal{CN}(0, P)$ is the input signal, P is the input power, and η is the HWIs distortion term. The term κ is the hardware quality factor that can be practically measured from the error vector magnitude (EVM) specified on the data sheets of the radio frequency (RF) transceivers, where $\kappa = 1 - \mathrm{EVM}^2$ [21].

Considering the worst situation, the HWIs are independent of the input and have a probability distribution corresponding

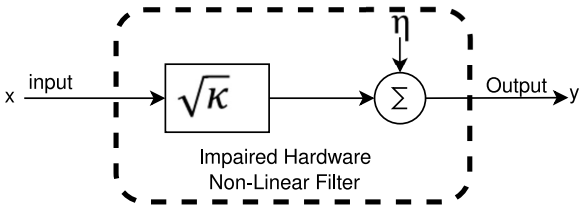

FIGURE 2. Hardware impairments modelling.

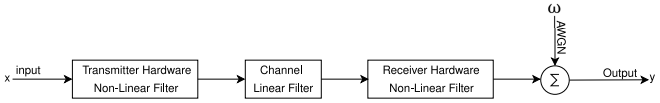

FIGURE 3. Hardware-impaired systems block diagram.

to $\eta \sim \mathcal{CN}(0, P(1-\kappa))$, and their power is proportional to the input power P by $(1-\kappa)$ constant. Worthy to note here is that the average power of the HWIs model's output equals its average input power. In other words, a fixed portion of the signal is turned into distortion. Thus, mathematically, $\mathbb{E}\{|y|^2\} = \kappa \mathrm{P} + (1-\kappa)\mathrm{P} = \mathrm{P}$ for $\kappa \in (0, 1]$.[1] Moreover, it is worth noting that the ideal hardware, i.e., $\kappa = 1$, leads to $\eta = 0$ and thus $y = x$.

B. SIGNAL MODEL

Considering the residual HWIs at the transceivers in both the BS and the MS, as depicted in Fig. 3, we can model both the impaired transmitter and the impaired receiver as will be discussed next.

1) THE HARDWARE IMPAIRED TRANSMITTER

Seeking to perform the joint localization-synchronization process and to track a mobile terminal, the BS broadcasts a well-known sequence as K OFDM symbols with power P utilizing N orthogonal subcarriers, G sequenced times. The OFDM symbols are presented as $\mathbf{z}^g[n] \in \mathbb{C}^{K\times 1} = [z_1^g[n], \ldots, z_K^g[n]]^{\mathrm{T}} \forall\ g,\ n$, where g and n present the indexes of the transmission and subcarrier, respectively. These symbols are transformed into the time domain, merged with a cyclic prefix (CP), and then precoded by the hybrid beamforming techniques.

The hybrid beamforming matrix $\mathbf{F}^g[n] \in \mathbb{C}^{M_{\mathrm{B}}\times k} = \mathbf{F}_{\mathrm{RF}}\mathbf{F}_{\mathrm{BB}}^g[n]$ at the transmitter is applied using a hybrid architecture to lower the hardware complexity, where $\mathbf{F}_{\mathrm{BB}}^g[n] \in \mathbb{C}^{L\times K}$ is the digital beamformer, L is the available chains at the BS, and $\mathbf{F}_{\mathrm{RF}} \in \mathbb{C}^{M_{\mathrm{B}}\times L}$ is implemented using analog phase shifters. Here, $[\mathbf{F}_{\mathrm{RF}}]_{(m,l)} = \mathrm{e}^{j\phi_{(m,l)}}$, while $\phi_{(m,l)}$ is a given phase for $m = 1, \ldots, M_{\mathrm{B}}$ and $l = 1, \ldots, L$ [34], [39].

The BS that suffers from HWIs broadcasts in the g^{th} transmission through the n^{th} subcarrier the following signal

$$\mathbf{s}^g[n] = \sqrt{\kappa_t}\mathbf{F}^g[n]\mathbf{z}^g[n] + \eta_t^g[n], \tag{10}$$

[1]The compensation algorithms that mitigate the HWIs maintain the average output power equal to the average of the input power [21]

where $\kappa_t \in (0, 1]$ is the transmitter hardware quality factor coefficient, and $\eta_t^g[n] \in \mathbb{C}^{M_{\mathrm{B}}\times 1}$ is the transmitter distortion term that is independent of $\mathbf{z}^g[n]$. The covariance matrix is denoted by $\Upsilon[n] = \mathbb{E}\{(\mathbf{F}^g[n]\mathbf{z}^g[n])(\mathbf{F}^g[n]\mathbf{z}^g[n])^{\mathrm{H}}\}$, where the average power $P = \mathrm{tr}(\Upsilon[n])$. Referring to the HWIs model, the distortion noise is given as $\eta_t^g[n] \sim \mathcal{CN}(\mathbf{0}, \Lambda[n])$, where $\Lambda[n] = (1-\kappa_t)\mathrm{diag}(\Upsilon_{11}[n], \ldots, \Upsilon_{M_{\mathrm{B}}M_{\mathrm{B}}}[n])$, and $\mathrm{tr}(\Lambda[n]) = P(1-\kappa_t)\ \forall n$. Accordingly,

$$\mathbb{E}\{\left(\mathbf{s}^g[n]\right)^{\mathrm{H}}\left(\mathbf{s}^g[n]\right)\} = \kappa_t P + (1-\kappa_t)P = P\ \forall n.$$

2) THE HARDWARE IMPAIRED RECEIVER

Following MS receiving the emitted signal from BS, it removes the CP and executes the fast Fourier transform (FFT). Then, the received signal through the LoS link over the n^{th} subcarrier at the g^{th} transmission time is

$$r_{\mathrm{LoS}}^g[n] = \sqrt{\kappa_t}(\mathbf{h}_0[n])^{\mathrm{T}}\mathbf{F}^g[n]\mathbf{z}^g[n] + (\mathbf{h}_0[n])^{\mathrm{T}}\eta_t^g[n], \tag{11}$$

whereas the received copy through the NLoS link over the n^{th} subcarrier at the g^{th} transmission time is given by

$$\begin{aligned} r_{\mathrm{NLoS}}^g[n] = {} & \sqrt{\kappa_t}(\mathbf{h}_1[n])^{\mathrm{T}}\Omega^g(\mathbf{H}_{\mathrm{r}}[n])^{\mathrm{T}}\mathbf{F}^g[n]\mathbf{z}^g[n] \\ & + (\mathbf{h}_1[n])^{\mathrm{T}}\Omega^g(\mathbf{H}_{\mathrm{r}}[n])^{\mathrm{T}}\eta_t^g[n]. \end{aligned} \tag{12}$$

The output of the imperfect transceiver of the MS is given according to the model in (9). Therefore, the MS's distorted signal by the HWIs and the additive white Gaussian noise (AWGN), i.e., $w^g[n] \sim \mathcal{CN}(0, \sigma^2)$, can be expressed as:

$$\begin{aligned} y^g[n] = {} & \sqrt{\kappa_t\kappa_r}(\mathbf{h}_0[n])^{\mathrm{T}}\mathbf{F}^g[n]\mathbf{z}^g[n] \\ & + \sqrt{\kappa_t\kappa_r}(\mathbf{h}_1[n])^{\mathrm{T}}\Omega^g(\mathbf{H}_{\mathrm{r}}[n])^{\mathrm{T}}\mathbf{F}^g[n]\mathbf{z}^g[n] \\ & + \sqrt{\kappa_r}(\mathbf{h}_1[n])^{\mathrm{T}}\Omega^g(\mathbf{H}_{\mathrm{r}}[n])^{\mathrm{T}}\eta_t^g[n] \\ & + \sqrt{\kappa_r}(\mathbf{h}_0[n])^{\mathrm{T}}\eta_t^g[n] + \eta_r^g[n] + w^g[n]. \end{aligned} \tag{13}$$

$\kappa_r \in (0, 1]$ presents the quality factor of the receiver hardware, and $\eta_r^g[n] \sim \mathcal{CN}(0, C_{\eta_r})$ represents the receiver HWIs distortion. Here, $C_{\eta_r} = P_{\mathrm{r}}(1-\kappa_r)$ presents the power of the receiver noise attributed to HWIs, and P_{r} is the input power to the MS, which equals

$$P_{\mathrm{r}} = P_{\mathrm{LoS}} + P_{\mathrm{NLoS}} = PM_{\mathrm{B}}\left(\rho_0^2 + M_{\mathrm{R}}^2\rho_{\mathrm{r}}^2\rho_1^2\right). \tag{14}$$

Specifically, $P_{\mathrm{LoS}} = PM_{\mathrm{B}}\rho_0^2$ is the power reaching the receiver over the LoS path, while $P_{\mathrm{NLoS}} = PM_{\mathrm{B}}M_{\mathrm{R}}^2\rho_{\mathrm{r}}^2\rho_1^2$ is the part of power passing to the receiver through the NLoS path. Besides, the BS causes $C_{\eta_t} = P\kappa_r(1-\kappa_t)M_{\mathrm{B}}(\rho_0^2 + M_{\mathrm{R}}^2\rho_{\mathrm{r}}^2\rho_1^2)$ distortion power at the MS side, and thus the distortion power accumulative at the receiver based on (13) is given by

$$\begin{aligned} C_y &= C_{\eta_t} + C_{\eta_r} + \sigma^2 \\ &= P(1-\kappa_t\kappa_r)M_{\mathrm{B}}\left(\rho_0^2 + M_{\mathrm{R}}^2\rho_{\mathrm{r}}^2\rho_1^2\right) + \sigma^2. \end{aligned} \tag{15}$$

Here, it is clear that C_y in (15) represents the power of the noisy signals in (13), while the noiseless part of (13) is

$$\begin{aligned} \varphi^g[n] = {} & \sqrt{\kappa_t\kappa_r} \times \\ & \left[(\mathbf{h}_0[n])^{\mathrm{T}} + (\mathbf{h}_1[n])^{\mathrm{T}}\Omega^g(\mathbf{H}_{\mathrm{r}}[n])^{\mathrm{T}}\right]\mathbf{F}^g[n]\mathbf{z}^g[n]. \end{aligned} \tag{16}$$

Accordingly, the signal-to-noise ratio (SNR) of the signal in (13) is

$$\mathrm{SNR} = \frac{\kappa_t \kappa_r M_{\mathrm{B}} \left(\rho_0^2 + M_{\mathrm{R}}^2 \rho_{\mathrm{r}}^2 \rho_1^2\right)}{(1 - \kappa_t \kappa_r) M_{\mathrm{B}} \left(\rho_0^2 + M_{\mathrm{R}}^2 \rho_{\mathrm{r}}^2 \rho_1^2\right) + \left(\sigma^2 / P\right)}, \quad (17)$$

and its asymptotic value when $P \to \infty$, i.e., the OFDM symbols power is high enough, is

$$\lim_{P \to \infty} \mathrm{SNR} = \frac{\kappa_t \kappa_r}{1 - \kappa_t \kappa_r}. \quad (18)$$

It is also worth mentioning here that when $\kappa_t = \kappa_r = 1$, i.e., the case of ideal hardware transceivers, the received signal in (13) becomes $y^g[n] = [(\mathbf{h}_0[n])^{\mathrm{T}} + (\mathbf{h}_1[n])^{\mathrm{T}} \Omega^g (\mathbf{H}_{\mathrm{r}}[n])^{\mathrm{T}}] \mathbf{F}^g[n] \mathbf{z}^g[n] + w^g[n]$, which consists only of the noiseless signal plus the white noise, where the variance of the received signal becomes $C_y = \sigma^2$, the variance of the AWGN. As such, the quality of the received signal is expressed by

$$\mathrm{SNR} = \frac{M_{\mathrm{B}} \left(\rho_0^2 + M_{\mathrm{R}}^2 \rho_{\mathrm{r}}^2 \rho_1^2\right)}{\left(\sigma^2 / P\right)}, \quad (19)$$

and thus $\lim_{P \to \infty} \mathrm{SNR} \to \infty$, which practically implies that, unlike the perfect systems with AWGN only, improving the quality of the received pilots by boosting the transmission power is bounded due to the existence of the HWIs.

IV. JOINT LOCALIZATION-SYNCHRONIZATION AND TRACKING

This section addresses the joint localization-synchronization processes along with the tracking performed by the single antenna MS. In specific, these processes are executed by observing the distortion of the pilot by the imperfect transceivers at both the MS and BS, as observed in the received signal from (13).

Accordingly, we first present the relationships between the parameters in (13) and the 3D coordinates of the RIS-aided *mm*wave MISO-OFDM system in Fig. 1. Then we execute the joint localization-synchronization process based on these relationships and the MLE, wherein its log-likelihood function is reformulated to consider the HWIs. Finally, we present the process of tracking a mobile terminal, which is carried out by the KFT implemented subsequent to the MLE stage. In this regard, the KFT is designed based on the errors in estimating the positions and according to the MS transition model.

A. GEOMETRIC FORMULATION

Fig. 4 depicts the relationships between the channel parameters in (13) and the 3D coordinates of the unknown position MS at $\mathbf{p}_{\mathrm{m}} = [\mathrm{p}_x,\ \mathrm{p}_y,\ \mathrm{p}_z]^{\mathrm{T}}$, the known position BS at $[\mathrm{b}_x,\ \mathrm{b}_y,\ \mathrm{b}_z]^{\mathrm{T}}$, and the known position RIS at $[\mathrm{r}_x,\ \mathrm{r}_y,\ \mathrm{r}_z]^{\mathrm{T}}$. According to Fig. 4, when the BS positions at the original point, without loss of generality, the geometric relationships can be expressed as follows

$$\tau_0 = \frac{\sqrt{\mathrm{p}_x^2 + \mathrm{p}_y^2 + \mathrm{p}_z^2}}{c} + \Delta, \qquad \psi_0 = \sin^{-1}\left(\frac{\sqrt{\mathrm{p}_x^2 + \mathrm{p}_y^2}}{\sqrt{\mathrm{p}_x^2 + \mathrm{p}_y^2 + \mathrm{p}_z^2}}\right),$$

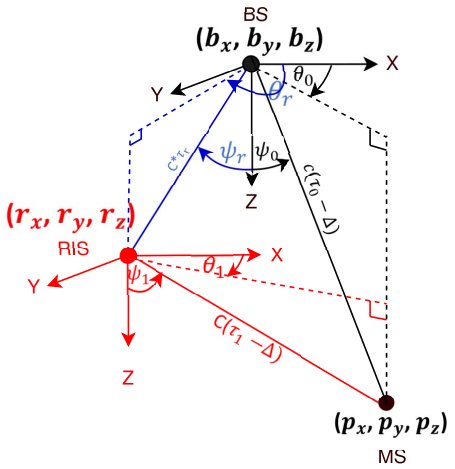

FIGURE 4. The RIS-aided *mm*wave MISO-OFDM system 3D coordinates.

$$\theta_0 = \mathrm{atan2}(\mathrm{p}_y, \mathrm{p}_x),$$
$$\tau_1 = \frac{\sqrt{(\mathrm{p}_x - \mathrm{r}_x)^2 + (\mathrm{p}_y - \mathrm{r}_y)^2 + (\mathrm{p}_z - \mathrm{r}_z)^2}}{c} + \Delta,$$
$$\psi_1 = \sin^{-1}\left(\frac{\sqrt{(\mathrm{p}_x - \mathrm{r}_x)^2 + (\mathrm{p}_y - \mathrm{r}_y)^2}}{\sqrt{(\mathrm{p}_x - \mathrm{r}_x)^2 + (\mathrm{p}_y - \mathrm{r}_y)^2 + (\mathrm{p}_z - \mathrm{r}_z)^2}}\right),$$
$$\theta_1 = \mathrm{atan2}\big((\mathrm{p}_y - \mathrm{r}_y), (\mathrm{p}_x - \mathrm{r}_x)\big). \quad (20)$$

It is clear that by having the BS and RIS placed at known and fixed positions, the $\mathbf{H}_r$ link's parameters are known constants, and can be given as

$$\tau_{\mathrm{r}} = \frac{\sqrt{\mathrm{r}_x^2 + \mathrm{r}_y^2 + \mathrm{r}_z^2}}{c}, \quad \psi_{\mathrm{r}} = \sin^{-1}\left(\frac{\sqrt{\mathrm{r}_x^2 + \mathrm{r}_y^2}}{\sqrt{\mathrm{r}_x^2 + \mathrm{r}_y^2 + \mathrm{r}_z^2}}\right),$$
$$\theta_{\mathrm{r}} = \mathrm{atan2}\big(\mathrm{r}_y, \mathrm{r}_x\big), \quad \bar{\psi}_{\mathrm{r}} = -\pi + \psi_{\mathrm{r}}, \quad \bar{\theta}_{\mathrm{r}} = -\pi + \theta_{\mathrm{r}}. \quad (21)$$

B. THE JOINT LOCALIZATION-SYNCHRONIZATION PROCESS

Due to the Gaussian white noise and the HWIs noises, the distorted pilot in (13) is Gaussian with mean $\varphi^g[n]$ and variance C_y defined in (15) and (16), respectively. As such, the channel parameters in the mean $\varphi^g[n]$ are unknowns, deterministic, and satisfy the geometric relationships in (20) for any position of the MS, $\mathbf{p}_{\mathrm{m}}$.

On the other side, the transmitted symbols and the beamforming matrix are known, and estimating the AWGN variance is possible for the initial access of *mm*wave systems [13], [34], [40]. Moreover, the values of the HWIs coefficients are obtained from the error vector magnitude (EVM) specified in the data sheets of RF components [21]. Furthermore, the channel parameters between the stationary BS and the stationary RIS are also deterministic, known, and calculated based on (21).

For this purpose, the MLE was chosen to estimate the position and clock drift of the MS, denoted as $[\mathbf{p}_{\mathrm{m}}\ ,\ \Delta]$,

respectively. According to the MLE rule, these parameters can be estimated through

$$\left(\hat{\mathbf{p}}_{\mathrm{m}},\ \hat{\Delta}\right) = \underset{\substack{\tau_0,\theta_0,\psi_0,\\ \tau_1,\theta_1,\psi_1}}{\arg\max} \left[\max_{\substack{\rho_0,\phi_0,\\ \rho_1,\phi_1}} L\begin{pmatrix}\tau_0,\theta_0,\psi_0,\rho_0,\phi_0,\\ \tau_1,\theta_1,\psi_1,\rho_1,\phi_1\end{pmatrix}\right],$$

where

$$L\begin{pmatrix}\tau_0,\theta_0,\psi_0,\rho_0,\phi_0,\\ \tau_1,\theta_1,\psi_1,\rho_1,\phi_1\end{pmatrix} = \log\left(f\left(\mathbf{y}\middle|\begin{matrix}\tau_0,\theta_0,\psi_0,\rho_0,\phi_0,\\ \tau_1,\theta_1,\psi_1,\rho_1,\phi_1\end{matrix}\right)\right)$$

represents the log-likelihood function of $\mathbf{y}$, which is the set of all observations for given τ_0, θ_0, ψ_0, ρ_0, ϕ_0, τ_1, θ_1, ψ_1, ρ_1 and ϕ_1 values, while $f(\cdot)$ is the probability density function (PDF) of $\mathbf{y}$. After some simple manipulations, the log-likelihood function of $\mathbf{y}$ can be written as

$$\begin{aligned} &L\begin{pmatrix}\tau_0,\theta_0,\psi_0,\rho_0,\phi_0,\\ \tau_1,\theta_1,\psi_1,\rho_1,\phi_1\end{pmatrix} \\ &= -\frac{NG}{2}\ln\left(2\pi\left(KP\left(\rho_0^2 + M_{\mathrm{R}}^2\rho_{\mathrm{r}}^2\rho_1^2\right)+\sigma^2\right)\right) \\ &\quad - \frac{\sum_{g=1}^{G}||\mathbf{y}^g - \sqrt{\kappa_t\kappa_r}\rho_0 e^{j\phi_0}\mathbf{w}_0^g - \sqrt{\kappa_t\kappa_r}\rho_1 e^{j\phi_1}\mathbf{w}_1^g||^2}{2\left(KP\left(\rho_0^2 + M_{\mathrm{R}}^2\rho_{\mathrm{r}}^2\rho_1^2\right)+\sigma^2\right)}, \end{aligned} \tag{22}$$

where $K = (1-\kappa_{\mathrm{t}}\kappa_{\mathrm{r}})M_{\mathrm{B}}$, and

$$\mathbf{y}^g = \left[y^g[0],\ldots,y^g[N-1]\right]^{\mathrm{T}},$$

as given in (13), while $\mathbf{w}_0^g$ and $\mathbf{w}_1^g$ are

$$\mathbf{w}_0^g = \begin{bmatrix} \alpha^{\mathrm{T}}(\theta_0,\psi_0,M_{\mathrm{B}})\mathbf{F}^g[0]\mathbf{z}^g[0] \\ \vdots \\ e^{-j2\pi[N-1]\frac{\tau_0}{NT}}\alpha^{\mathrm{T}}(\theta_0,\psi_0,M_{\mathrm{B}})\mathbf{F}^g[N-1]\mathbf{z}^g[N-1] \end{bmatrix},$$

$$\mathbf{w}_1^g = \begin{bmatrix} \alpha^{\mathrm{T}}(\theta_1,\psi_1,M_{\mathrm{R}})\Omega^g\mathbf{H}_{\mathrm{r}}^{\mathrm{T}}[0]\mathbf{F}^g[0]\mathbf{z}^g[0] \\ \vdots \\ e^{-j2\pi[N-1]\frac{\tau_1}{NT}}\alpha^{\mathrm{T}}(\theta_1,\psi_1,M_{\mathrm{R}})\Omega^g\mathbf{H}_{\mathrm{r}}^{\mathrm{T}}[N-1]\mathbf{F}^g[N-1]\mathbf{z}^g[N-1] \end{bmatrix}. \tag{23}$$

According to the derivation in Appendix A, the log-likelihood function of $\mathbf{y}$ can be rewritten in terms of τ_0, θ_0, ψ_0,τ_1, θ_1 and ψ_1 as in the top of the next page. where c_{00}, c_{01}, c_{10}, and c_{11} are defined in Appendix A.

Unfortunately, (24) cannot be represented in any projection matrix and does not have a closed-form solution either. Moreover, it is highly non-linear and exhibits several local minima. Accordingly, a numerical search algorithm is used to maximize this cost function. Specifically, a 4D grid search algorithm over the space of $[\mathbf{p}_{\mathrm{m}}\ ,\ \Delta] = [\mathrm{p}_x,\ \mathrm{p}_y,\ \mathrm{p}_z,\ \Delta]$ is employed to find the optimal point. At each point over the 4D search grid, the values are converted to the channel parameters $[\tau_0,\theta_0,\psi_0,\tau_1,\theta_1,\psi_1]$ according to (20), and then fed into the cost function. The optimal point, representing the estimated position and clock offset $[\hat{\mathbf{p}}_{\mathrm{m}}\ ,\ \hat{\Delta}]$, is the one that maximizes the cost function. It is important to note that works such as [12], [13], [34] presented adequate initialization and low complex approaches to overcome the burden of multidimensional optimization.

C. KALMAN FILTER BASED TRACKING PROCESS

This subsection aims to track a mobile terminal that moves between two consecutive positions, $\mathbf{p}_{\mathrm{m}}(t-1)$ and $\mathbf{p}_{\mathrm{m}}(t)$, according to the Gaussian transition model. Here, with the mobile terminal scenario, we append the independent variable t to the equations to refer to the values at the t^{th} position sample. The MLE localizes the MS by optimizing (24) at each sample, and then each estimated position is fed into the KFT. Concerning the KFT, its matrices are determined depending on the transition model of the MS and on the localization accuracy harmed by the HWIs.

Initially, it is self-evident that the estimated position $\hat{\mathbf{p}}_{\mathrm{m}}$ in the previous subsection is a noisy version of the real $\mathbf{p}_{\mathrm{m}}$. Therefore,

$$\hat{\mathbf{p}}_{\mathrm{m}}(t) = \mathbf{p}_{\mathrm{m}}(t) + \mathbf{w}(t), \tag{25}$$

where the vector $\mathbf{w}(t) \in \mathbb{R}^{3\times 1}$ presents the localization process error at the t^{th} position sample with the covariance matrix $\mathbf{C}(t) \in \mathbb{R}^{3\times 3}$.

In developing a model for the dynamics of MS mobility, we consider the MS's maneuvers as it changes its position, moving with variable rates and steps. These steps can be affected by minor unintended position adjustments, street obstructions, wind gusts, and other factors. The change in the position of the MS can be modeled as a zero-mean Gaussian random variable with variance depending on the physical capabilities in the change in the velocity components from sample to sample [19], [41], [42]. Accordingly, the difference between two successive positions at any two adjacent samples is modeled as independent Gaussian noise. Thus, the Markov state transition model introduced for the successive MS tracking problem is given as

$$\mathbf{p}_{\mathrm{m}}(t) = \mathbf{p}_{\mathrm{m}}(t-1) + \mathbf{u}(t), \tag{26}$$

where $\mathbf{u}(t) \sim \mathcal{N}(\mathbf{0},\mathbf{Q})$, $\mathbf{Q} = \mathrm{diag}([\sigma_x^2,\sigma_y^2,\sigma_z^2])$, and the values of σ_x^2, σ_y^2, and σ_z^2 should depend on the possible change in the position components from sample to sample. Thus, based on (26), the conditional probability of $\mathbf{p}_{\mathrm{m}}(t)$ given $\mathbf{p}_{\mathrm{m}}(t-1)$ is

$$p(\mathbf{p}_{\mathrm{m}}(t)|\mathbf{p}_{\mathrm{m}}(t-1)) \sim \mathcal{N}(\mathbf{p}_{\mathrm{m}}(t-1),\mathbf{Q}). \tag{27}$$

Moreover, according to [19], for any two samples $t \neq t'$, $\mathbf{u}(t)$ and $\mathbf{u}(t')$ are independent, and thus the user positions $p_{\mathrm{m}}(t)$ form a Markov chain satisfying

$$p(\mathbf{p}_{\mathrm{m}}(t)|\mathbf{p}_{\mathrm{m}}(0{:}t-1)) = p(\mathbf{p}_{\mathrm{m}}(t)|\mathbf{p}_{\mathrm{m}}(t-1)), \tag{28}$$

where $\mathbf{p}_{\mathrm{m}}(0{:}t-1)$ is the collection of user positions from the first sample to the $t-1$ samples.

Now, it is clear that (26) evolves according to the Gauss-Markov model, while (25) represents the observation vector that is modelled by the Bayesian linear model. Accordingly, the tracking of $\mathbf{p}_{\mathrm{m}}(t)$ can be implemented sequentially based on $\hat{\mathbf{p}}_{\mathrm{m}}(0{:}t)$ observations and using the Kalman filter described in Appendix B for a nonstationary signal.

V. BAYESIAN CRAMER-RAO BOUND

This section presents the best achievable accuracy of the tracking process in a 3D RIS-aided *mm*wave MISO-OFDM system, suffering from the HWIs at the transceivers of both the MS and BS. Initially, this section introduces the FIM that measures the amount of information obtained from the observations in (13). Next, it formulates the BFIM by considering the priori information in (27) simultaneously with the information obtained from the observations. The BCRB benchmark used to evaluate the tracking of a non-stationary MS in the RIS-aided *mm*waveMISO-OFDM system affected by HWIs, is the inverse of the BFIM. The optimal achievable accuracy for the joint localization-synchronization process, in terms of the CRB, was previously derived in [33].

A. OBSERVATIONS FIM

Let us start by defining the vector of downlink channel parameters, given as $\beta = [\tau_0,\ \theta_0,\ \psi_0,\ \rho_0,\ \phi_0,\ \tau_1,\ \theta_1,\ \psi_1,\ \rho_1,\ \phi_1]^{\mathrm{T}}$ and the vector of localization parameter as $\mu = [\mathrm{p}_x,\ \mathrm{p}_y,\ \mathrm{p}_z,\ \Delta]^{\mathrm{T}}$. The elements of the FIM $\mathbf{J}_\beta \in \mathbb{R}^{10\times 10}$, which measures the amount of information about β obtained from observing $y^g[n]$ in (13), are given according to

$$\left[\mathbf{J}_\beta\right]_{(i,j)} = 2\sum_{g=1}^{G}\sum_{n=0}^{N-1}\Re\left\{\left(\frac{\partial\varphi^g[n]}{\partial\beta_i}\right)^{\mathrm{H}} C_y^{-1}\left(\frac{\partial\varphi^g[n]}{\partial\beta_j}\right)\right\} + \mathrm{tr}\left(C_y^{-1}\frac{\partial C_y}{\partial\beta_i}C_y^{-1}\frac{\partial C_y}{\partial\beta_j}\right). \tag{29}$$

β_i and β_j represent the i^{th} and j^{th} parameters of vector β, respectively, and $\varphi^g[n]$ is the noiseless signal given in (16). C_y is the noise variance defined in (15), and the elements of $\mathbf{J}_\beta$ are defined in greater detail in Appendix C.

Following that, the FIM of the position parameters vector $\mathbf{J}_\mu \in \mathbb{R}^{4\times 4}$ is calculated according to the following transformation formula $\mathbf{J}_\mu = \mathbf{T}\mathbf{J}_\beta\mathbf{T}^{\mathrm{T}}$, where the transformation matrix,$\mathbf{T} \in \mathbb{R}^{4\times 10}$, is defined by

$$\mathbf{T} \overset{(\text{def})}{=} \frac{\partial\beta^{\mathrm{T}}}{\partial\mu}, \tag{30}$$

and the elements of the transformation matrix $\mathbf{T}$ are derived in Appendix D.

B. BFIM

When the MS transits to a new location $\mathbf{p}_{\mathrm{m}}(t) = [\mathrm{p}_x(t),\ \mathrm{p}_y(t),\ \mathrm{p}_z(t)]^{\mathrm{T}}$ at a given t^{th} sample, the vectors and matrices $\beta, \mathbf{J}_\beta, \mathbf{T}, \mu$ and $\mathbf{J}_\mu$, that depend on MS location, change from their previous state to a new one. Consequently, at each sample, $\beta(t)$, $\mathbf{J}_\beta(t)$ and $\mathbf{T}(t)$ are updated according to (20), (29) and Appendix D, respectively. Moreover, the FIM of the $\mu(t)$ in the given t^{th} sample is updated as follows

$$\mathbf{J}_\mu(t) = \mathbf{T}(t)\mathbf{J}_\beta(t)\mathbf{T}^{\mathrm{T}}(t)\ \forall t. \tag{31}$$

According to [43] and [19], for an arbitrary t sample, the BFIM of $\mu(t)$ vector, $\mathbf{J}_\mu^{(\mathrm{B})}(t) \in \mathbb{R}^{4\times 4}$, can be decomposed into two additive parts. The first part represents the information obtained from the observations in (13), while the second part represents the priori information in (27). Consequently, the BFIM is recursively calculated by

$$\mathbf{J}_\mu^{(\mathrm{B})}(t) = \underbrace{\mathbf{J}_\mu(t)}_{\text{Observations}} + \underbrace{\mathbf{G}_{22}(t) - \mathbf{G}_{21}(t)\left[\mathbf{J}_\mu^{(\mathrm{B})}(t-1) + \mathbf{G}_{11}(t)\right]^{-1}\mathbf{G}_{12}(t)}_{\text{Priori Information}}, \tag{32}$$

where the superscript (B) refers to Bayesian,

$$\begin{aligned}
\mathbf{G}_{11}(t) &= \mathbb{E}\left\{-\frac{\partial^2\log p\Big(\mu(t)|\mu(t-1)\Big)}{\partial\mu(t-1)\Big(\partial\mu(t-1)\Big)^{\mathrm{T}}}\right\},\\
\mathbf{G}_{12}(t) &= \mathbb{E}\left\{-\frac{\partial^2\log p\Big(\mu(t)|\mu(t-1)\Big)}{\partial\mu(t-1)\Big(\partial\mu(t)\Big)^{\mathrm{T}}}\right\},\\
\mathbf{G}_{21}(t) &= \mathbb{E}\left\{-\frac{\partial^2\log p\Big(\mu(t)|\mu(t-1)\Big)}{\partial\mu(t)\Big(\partial\mu(t-1)\Big)^{\mathrm{T}}}\right\},\\
\mathbf{G}_{22}(t) &= \mathbb{E}\left\{-\frac{\partial^2\log p\Big(\mu(t)|\mu(t-1)\Big)}{\partial\mu(t)\Big(\partial\mu(t)\Big)^{\mathrm{T}}}\right\},
\end{aligned} \tag{33}$$

and $\mathbf{J}_\mu(t)$ is expressed in (31).

Since the parameter Δ is constant over the different samples, then

$$p\Big(\mu(t)|\mu(t-1)\Big) = p\Big(\mathbf{P}(t)|\mathbf{P}(t-1)\Big). \tag{34}$$

The logarithmic expression of the right side of (34), considering (27), equals

$$\log p\Big(\mathbf{P}(t)|\mathbf{P}(t-1)\Big) = -\frac{3}{2}\log 2\pi - \frac{1}{2}\log|\mathbf{Q}| - \frac{1}{2}\Big[(\mathbf{P}(t)-\mathbf{P}(t-1))^{\mathrm{T}}\mathbf{Q}^{-1}(\mathbf{P}(t)-\mathbf{P}(t-1))\Big],$$

$$L(\tau_0,\theta_0,\psi_0\tau_1,\theta_1,\psi_1) = -\frac{NG}{2} - \frac{NG}{2}\ln\left(\frac{2\pi}{NG}\sum_{g=1}^{G}\left\|\mathbf{y}^g - \frac{c_{11}\sum_{i=1}^{G}\left(\mathbf{w}_0^i\right)^{\mathrm{H}}\mathbf{y}^i - c_{01}\sum_{i=1}^{G}\left(\mathbf{w}_1^i\right)^{\mathrm{H}}\mathbf{y}^i}{c_{00}c_{11}-c_{01}c_{10}}\mathbf{w}_0^g - \frac{c_{00}\sum_{i=1}^{G}\left(\mathbf{w}_1^i\right)^{\mathrm{H}}\mathbf{y}^i - c_{10}\sum_{i=1}^{G}\left(\mathbf{w}_0^i\right)^{\mathrm{H}}\mathbf{y}^i}{c_{00}c_{11}-c_{01}c_{10}}\mathbf{w}_1^g\right\|^2\right). \tag{24}$$

and consequently,

$$\mathbb{E}\left\{-\frac{\partial^2 \log p\Big(\mathbf{P}(t)|\mathbf{P}(t-1)\Big)}{\partial \mathbf{P}(t-1)(\partial \mathbf{P}(t-1))^{\mathrm{T}}}\right\} = \mathbf{Q}^{-1}.$$

Considering the definitions of the $\mathbf{G}$ matrices in (33), $\mathbf{G}_{11}(t) = \mathbf{G}_{22}(t) = -\mathbf{G}_{12}(t) = -\mathbf{G}_{21}(t) \in \mathbb{R}^{4\times 4}$, where

$$\mathbf{G}_{11}(t) = \begin{bmatrix} \mathbf{Q}^{-1} & 0 \\ 0 & 0 \end{bmatrix},$$

Now, by initializing $\mathbf{J}_{\mu}^{(\mathrm{B})}(0) = \mathbb{E}\left\{-\frac{\partial^2 \log p\Big(\mathbf{P}(0)\Big)}{\partial \mathbf{P}(0)(\partial \mathbf{P}(0))^{\mathrm{T}}}\right\}$, the BCRB of the estimation of $\mu(t)$ at the t^{th} sample is given by computing the inverse of $\mathbf{J}_{\mu}^{(\mathrm{B})}(t)$.

VI. SIMULATION RESULTS

This section conducts numerical experiments to discuss the joint localization-synchronization process and tracking in the 3D RIS-aided *mm*wave MISO-OFDM system under the harmful effects of the HWIs. We consider the same simulation settings and scenarios assumed in the literature, as in [34] and [13] when studying the localization with ideal transceivers, or investigating the case of the localization with HWIs, such as in [25], [30], [33].

A. SIMULATION SETTINGS

Within these simulations, the BS broadcasts a well-known signal over $K = 1$ simultaneous beams, $G = 20$ times. This signal is broadcasted over a carrier of $f_c = 60$ GHz frequency, $B = 40$ MHz bandwidth that is divided upon $N = 20$ subcarriers. Moreover, in this system, the narrowband condition is assumed as the bandwidth and subcarriers achieve $\lambda_1 = \lambda_2 = \cdots \lambda_{20} \approx \lambda_c = 5$ mm.

The single antenna MS at any unknown position receives two copies of the known signal. The first copy reaches directly from the BS located at the origin $q = [0, 0, 0]$ m and is equipped with $M_{\mathrm{B}} = 16$ antennas. The second copy is received through the $M_{\mathrm{R}} = 36$ elements RIS, which is located at a known position in $r = [0.2, 8, 0.5]$ m and generates the phase control matrix (Ω^g) by assuming equiprobable binary random variables. In the context of the joint localization-synchronization process, the MS is located in $p = [7,\ 7,\ 2]$ m. Subsequently, following the literature in [13], the channel amplitudes, ρ_0, ρ_1, ρ_r, are generated according to the common path loss model in free space as: $\rho_0 = \lambda_c/(4\pi\|p\|)$, $\rho_1 = \lambda_c/(4\pi\|p - r\|)$, and $\rho_r = \lambda_c/(4\pi\|r\|)$. Besides, the channel phase ϕ_0, ϕ_1, and ϕ_r are selected as $\pi/6, \pi/3$, and $\pi/4$, respectively. The azimuth and elevation AoD, and ToF are calculated by substituting the coordinates q, r, and p in the geometrical relationship in (20).

It is important to note that the two copies of the pilot are distorted by the transceivers of the BS and MS, as the transceivers are non-ideal and suffer from HWIs. For simplicity, these transceivers have distortion coefficients of $\kappa_t = \kappa_r = \kappa$, and their clocks exhibit a drift of $\Delta = NT/8 = 62.5$ ns.

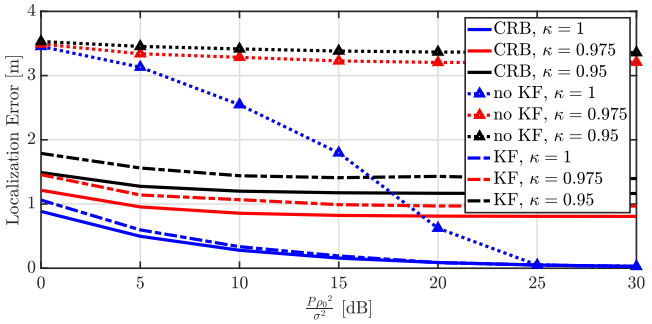

FIGURE 5. Localization error and CRB v.s the transmission power with different κ.

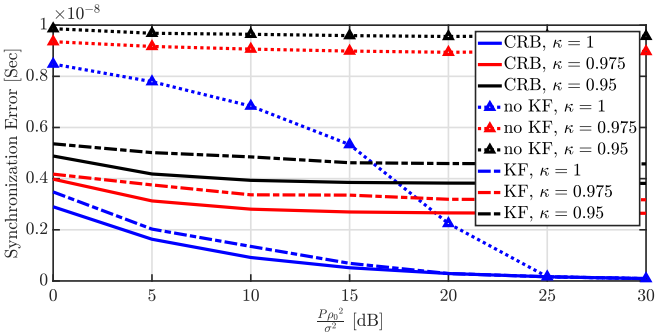

FIGURE 6. Synchronization error and CRB v.s the transmission power with different κ.

Subsequently, within the same system and under identical settings, the MS is assumed to initiate from the position $[7,\ 7,\ 2]$ and maneuver through 300 positions. This mobility adheres to the transition model $p(\mathbf{p}_{\mathrm{m}}(t)|\mathbf{p}_{\mathrm{m}}(t-1)) \sim \mathcal{N}(\mathbf{p}_{\mathrm{m}}(t-1), \mathbf{Q})$. Moreover, it is assumed that the average movement distance of the MS between adjacent samples is determined by $\mathbf{Q} = \mathrm{diag}([0.03,\ 0.07,\ 0.01])$ accomplishing $\mathbb{E}\{\|\mathbf{p}_{\mathrm{m}}(t) - \mathbf{p}_{\mathrm{m}}(t-1)\|\} = \sqrt{0.11}$ m.

B. THE JOINT LOCALIZATION-SYNCHRONIZATION PROCESS DISCUSSION

This subsection evaluates the joint localization-synchronization process, which relies on receiving two copies of the pilot distorted by the HWIs noises, where the detrimental effect of the HWIs is presented in Fig. 5 and Fig. 6. Specifically, these figures compare the empirical and theoretical accuracies of the joint localization-synchronization process,i.e., "no KF" and "KF" cases, in terms of the root mean squared error (RMSE) and CRB across different values of κ and $\frac{P\rho_0^2}{\sigma^2}$. It should be noted that the CRB term is the analytical performance metric, whereas the RMSE, used to evaluate the performance, is computed using Monte Carlo simulations.

Increasing the HWIs of the transceivers deteriorates the received signal quality, leading to a less accurate joint localization-synchronization process, as clearly depicted in the figures. Moreover, the figures show that generally

boosting the transmission power to improve the quality of the received signal enhances the accuracy of the joint localization-synchronization process. Unfortunately, these accuracy enhancements are limited to a certain level when the hardware qualities of the transceivers are imperfect.

When the transceivers are ideal (i.e., $\kappa = 1$), it's noted that increasing transmission power leads the errors to approach zero, while the existence of the HWIs bounds the position and synchronization to higher than zero errors. It's clear that the non-noisy signal $\varphi^g[n]$ in (16) and the power of the HWIs distortion C_y in (15) increase simultaneously with the increase of the transmission power. As a result of increasing the HWIs distortion C_y proportionally with power, the HWIs are humble with small power values. Consequently, the figure shows that the differences between the accuracy of the processes associated with the different κ values are negligible at a small transmission range of power, while the accuracy differences become notable as the transmission power increases.

Moreover, it is evident that the RMSE converges to the CRB when $\frac{P\rho_0^2}{\sigma^2} \geq 25$ dB in the scenario with the ideal transceiver. Consequently, the SNR in (19) also exceeds 25 dB. This observed behaviour is attributed to the properties of the MLE. Particularly, when the number of measurements is limited -as is the case in this work- the accuracy of the MLE approaches the CRB for sufficiently high SNR values [41]. In the case of non-ideal hardware, according to (18), the SNR saturates at 12.85 dB and 9.66 dB when $\kappa = 0.975$ and 0.95, respectively. These values lie below the SNR threshold required for the RMSE to meet the PEB and SEB standards.

Additionally, the proposed methodologies, as depicted in Fig. 5 and Fig. 6, employ a KF with MC techniques, (KF) case in the figures, to improve the accuracy of the joint localization-synchronization process. These figures showcase a notable improvement in accuracy, with smaller deviations from the theoretical benchmark, attributed to the integration of KF with MC. Specifically, following the estimation of the MS's position and clock offset, the KF, detailed in the Appendix B, processes the estimated values. To achieve this, we set the $\mathbf{Q}$ in (39b) as a zero matrix, since it is a fixed MS's position scenario. Concerning the role of MC in mitigating HWIs influence, it offers a precise description for $\mathbf{C}(t)$ in (39c). Further details regarding the MC approach are discussed in the subsequent subsection.

Figures 7 and 8 illustrate the comparison between the impact of employing the optimal phase control matrix and a random phase control matrix concerning localization and synchronization errors. This comparison assumes the availability of the optimal phase-shift control matrix at the RIS before initiating the processes. The figures reveal limited enhancement, and this can be attributed to two main reasons. Firstly, in the presence of both LoS and NLoS, the LoS link provides the most valuable information for the joint localization-synchronization and tracking process.

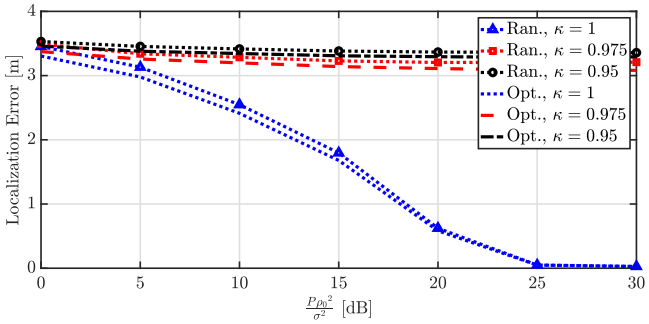

FIGURE 7. Optimal phase control matrix v.s random phase control matrix comparison in terms of localization error.

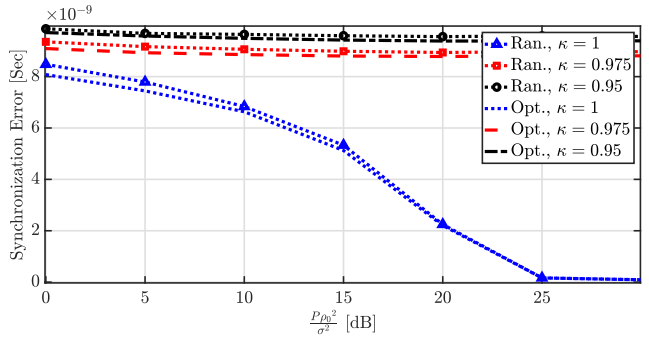

FIGURE 8. Optimal phase control matrix v.s random phase control matrix comparison in terms of synchronization error.

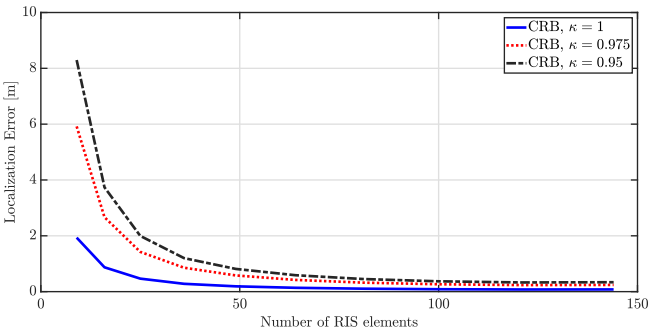

FIGURE 9. PEB v.s the number of RIS elements with different κ.

Consequently, improving the quality of NLoS through the use of the optimal phase-shift control matrix results in only marginal accuracy improvement. Additionally, as the transmitted power increases, the difference in accuracy between the two matrices diminishes, primarily because the dominant enhancement is achieved through the LoS, rather than the NLoS. Secondly, in the scenario of an imperfect transceiver, enhancing the NLoS link quality not only amplifies the useful signal power but also increases the power of HWIs. This dual impact contributes to the limited effectiveness of the optimal phase-shift control matrix in improving accuracy.

In the same context, the precision of the joint localization-synchronization procedure is illustrated in Fig. 9 and Fig. 11, delineating the accuracy in terms of PEB and SEB. These

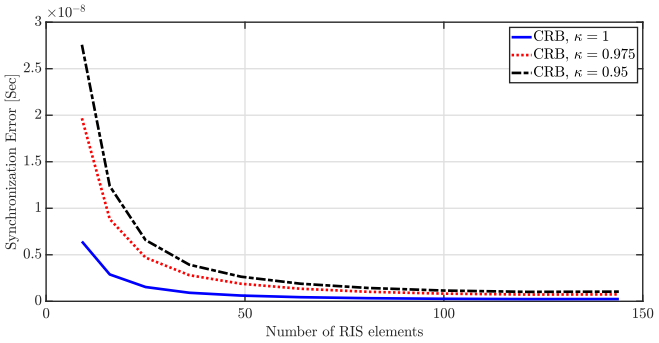

FIGURE 10. SEB v.s the number of RIS elements with different κ.

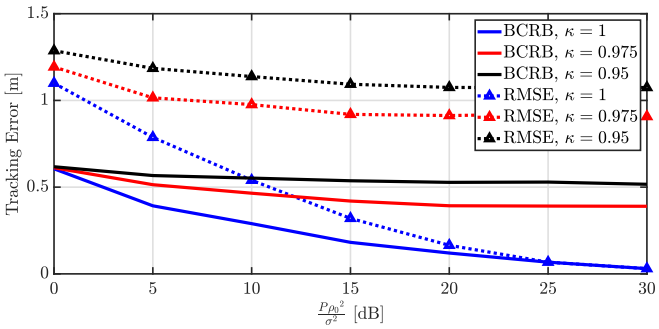

FIGURE 11. Tracking error and BCRB v.s the transmission power with different κ.

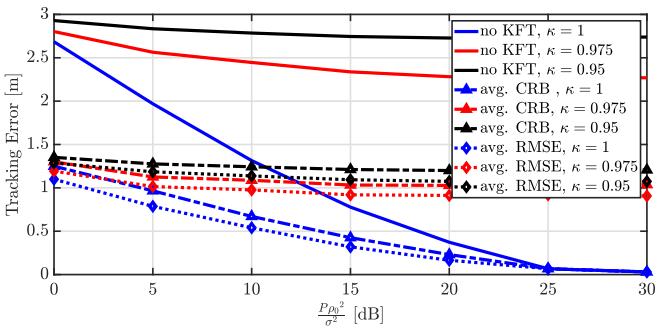

FIGURE 12. Tracking error and BCRB v.s. the transmission power with different C matrix and κ.

visuals demonstrate that as the count of RIS elements grows, the accuracy of the joint localization-synchronization noticeably improves. Particularly, within a range of a small number of RIS elements, a slight increase in their quantity significantly enhances accuracy.

C. THE TRACKING PROCESS DISCUSSION

This subsection investigates the accuracy of the KFT of a mobile terminal described above in the simulation settings subsection, where the tracking process at each t position sample consists of two phases. In the first phase, the MS is localized at the t^{th} position as in the joint localization-synchronization process in (24). Next, in the second phase, the MS is tracked at that t^{th} position by implementing the KFT on the t^{th} output resulting from the first phase.

Fig. 11 presents the accuracy of the tracking process for different values of κ when the $\mathbf{C}$ matrix, the matrix that

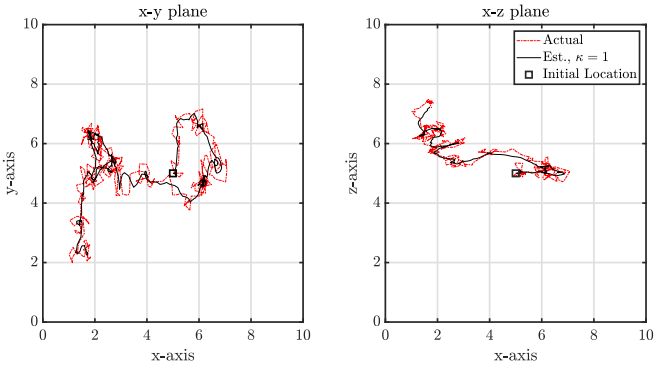

FIGURE 13. The estimated trajectory of the ideal transceivers scenario.

describes the errors in the estimated position, is determined based on the MC method. As the HWIs noise, denoted by κ, increases, the tracking accuracy, evaluated in terms of both BCRB and RMSE, worsens. This trend is consistent with the observations made for the joint localization-synchronization process. Conversely, when the HWIs noise is diminished by reducing the transmitted data power, thereby resulting in a lower $\frac{P\rho_0^2}{\sigma^2}$ value, the accuracy of the tracking process remains relatively stable across different κ values.

Moreover, it is clear that in the case of ideal hardware, the accuracy of the tracking process in terms of RMSE can match the theoretical BCRB when the quality of the received signal is sufficiently high. Conversely, the presence of non-ideal hardware imposes a saturation limit on the tracking accuracy, mirroring the impact observed on the foundational localization process. Fortunately, the more appropriate selection of the $\mathbf{C}$ matrix helps the KFT compensate for the lack of accuracy, as illustrated in Fig. 15.

Fig. 15 presents the accuracy of the tracking process in terms of RMSE, with different κ and $\mathbf{C}$ matrix values. Firstly, the figure plots the accuracy of the tracking process without implementing the KFT, the raw output of the localization process, which is denoted as *no KFT*. Concurrently, the figure presents two scenarios, where KFT is applied. In the first scenario, labeled as the *avg. CRB*, the $\mathbf{C}$ matrix represents the average of the CRBs of the localization processes. In the second scenario, termed the *avg. RMSE*, the $\mathbf{C}$ matrix is derived from the average of the RMSE of the localization processes based on the MC approach.

In Fig. 15, a significant enhancement in tracking accuracy due to the KFT is observed for both impaired and ideal transceivers. Regarding the perfect transceivers, the impact of the KFT becomes more significant at low quality received pilots, i.e., the range of small $\frac{P\rho_0^2}{\sigma^2}$ values, but no difference in the tracking accuracy at the range of high $\frac{P\rho_0^2}{\sigma^2}$ values. More interestingly, in the case of non-ideal transceivers, the KFT improves the tracking accuracy across the entire $\frac{P\rho_0^2}{\sigma^2}$ range.

Moreover, Fig. 15 indicates that selecting the $\mathbf{C}$ matrix that represents the accuracy of the localization process, affects the accuracy of the tracking process. In other words, this figure

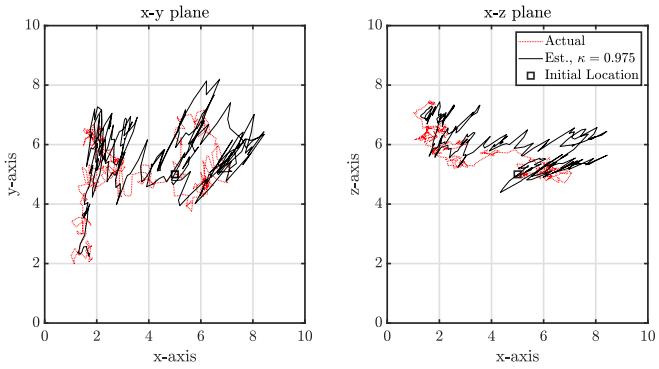

FIGURE 14. The estimated trajectory of the imperfect transceivers scenario.

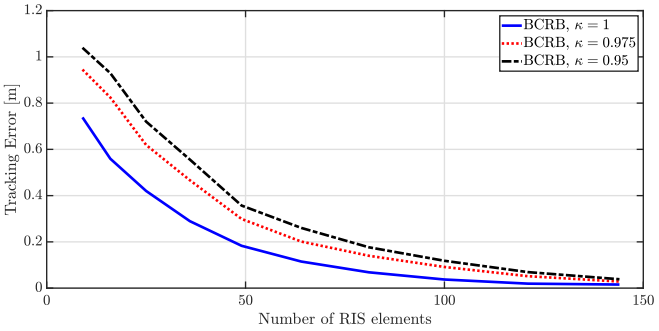

FIGURE 15. BCRB v.s the number of RIS elements with different κ.

shows that the accuracy of the tracking process of the *avg. CRB* scenario is inferior to the *avg. RMSE* scenario. This is because the MC approach yields a more realistic covariance matrix $\mathbf{C}$ compared to the *avg. CRB* case, where the matrix $\mathbf{C}$ in the *avg. CRB* case represents an unattainable localization process accuracy due to the HWIs or an insufficiently high value of $\frac{P\rho_0^2}{\sigma^2}$ in the ideal case. However, when the $\frac{P\rho_0^2}{\sigma^2}$ value is sufficiently high, there is no discernible difference in accuracy between the *avg. CRB* case and the *avg. RMSE* case, and their accuracy equals the accuracy of the *no KFT* case.

Figures 13 and 14 present a comparison between the estimated trajectories in scenarios featuring ideal and imperfect transceivers. These visualizations depict the 3D trajectory projections on the x-y and x-z planes. The comparison, conducted over 300 samples, reveals that the tracking process yields a trajectory closer to the intended path in the ideal transceivers scenario compared to the imperfect transceivers scenario.

The analysis of tracking accuracy concerning the number of RIS elements is explored in Fig. 10, focusing on BCRB terms. The figure demonstrates that augmenting the quantity of RIS elements results in improved tracking accuracy. In cases with a small number of RIS elements, noticeable disparities in accuracy exist between ideal and imperfect transceivers. However, as the number of RIS elements increases into the higher range, these differences diminish, and the accuracy of both ideal and imperfect transceivers converges.

VII. CONCLUSION

In this work, a single antenna MS performs the joint localization-synchronization process and tracking in the 3D RIS-aided *mm*wave MISO-OFDM systems. The MS continuously observes the BS broadcasting a well-known pilot, distorted by the non-ideal hardware of both the MS and BS. Subsequently, the joint localization-synchronization process is executed based on these observations and by maximizing the MLE cost function, which considers the perfect and the impaired transceiver cases. This stage evaluates the drift between the BS and MS clocks and jointly estimates the user coordinates, which serve as inputs for the KFT for tracking purposes in the mobile terminal scenario. The KFT is designed considering the localization accuracy degradation caused by the HWIs and the terminal transition model. For assessment purposes, the BCRB is derived to evaluate the tracking process. Our simulation results depict the deterioration in the accuracy of the joint localization-synchronization process and tracking because of HWIs at the BS and MS. Furthermore, the results reveal that the HWIs distortion prevents the joint localization-synchronization process and the tracking from achieving the theoretical bounds even though it is possible with ideal transceivers. Fortunately, a more realistic covariance matrix description via MC technique upgrades the accuracy of the tracking process achieving closer accuracy to the theoretical bound.

APPENDIX A
MLE DERIVATION

It is evident that the estimated values of ϕ_0 and ϕ_1 that maximize (22) can be given as

$$\frac{\partial L(\tau_0,\theta_0,\psi_0,\rho_0,\phi_0,\tau_1,\theta_1,\psi_1,\rho_1,\phi_1)}{\partial\phi_0} = \frac{\sum_{g=1}^{G}\left(\mathbf{w}_0^g\right)^{\mathrm{H}}\left(\mathbf{y}^g-\sqrt{\kappa_t\kappa_r}\rho_0 e^{j\phi_0}\mathbf{w}_0^g-\sqrt{\kappa_t\kappa_r}\rho_1 e^{j\phi_1}\mathbf{w}_1^g\right)}{\frac{KP\left(\rho_0^2+M_{\mathrm{R}}^2\rho_{\mathrm{r}}^2\rho_1^2\right)+\sigma^2}{1/j\sqrt{\kappa_t\kappa_r}\rho_0 e^{j\phi_0}}} = 0,$$

$$\frac{\partial L(\tau_0,\theta_0,\psi_0,\rho_0,\phi_0,\tau_1,\theta_1,\psi_1,\rho_1,\phi_1)}{\partial\phi_1} = \frac{\sum_{g=1}^{G}\left(\mathbf{w}_1^g\right)^{\mathrm{H}}\left(\mathbf{y}^g-\sqrt{\kappa_t\kappa_r}\rho_0 e^{j\phi_0}\mathbf{w}_0^g-\sqrt{\kappa_t\kappa_r}\rho_1 e^{j\phi_1}\mathbf{w}_1^g\right)}{\frac{KP\left(\rho_0^2+M_{\mathrm{R}}^2\rho_{\mathrm{r}}^2\rho_1^2\right)+\sigma^2}{1/j\sqrt{\kappa_t\kappa_r}\rho_1 e^{j\phi_1}}} = 0,$$

where after mathematical manipulation, the above equations become

$$\left(\rho_0\sum_{g=1}^{G}\left(\mathbf{w}_0^g\right)^{\mathrm{H}}\mathbf{w}_0^g\right)e^{j\phi_0}+\left(\rho_1\sum_{g=1}^{G}\left(\mathbf{w}_0^g\right)^{\mathrm{H}}\mathbf{w}_1^g\right)e^{j\phi_1} = \frac{\sum_{g=1}^{G}\left(\mathbf{w}_0^g\right)^{\mathrm{H}}\mathbf{y}^g}{\sqrt{\kappa_t\kappa_r}},$$

$$\left(\rho_0\sum_{g=1}^{G}\left(\mathbf{w}_1^g\right)^{\mathrm{H}}\mathbf{w}_0^g\right)e^{j\phi_0}+\left(\rho_1\sum_{g=1}^{G}\left(\mathbf{w}_1^g\right)^{\mathrm{H}}\mathbf{w}_1^g\right)e^{j\phi_1} = \frac{\sum_{g=1}^{G}\left(\mathbf{w}_1^g\right)^{\mathrm{H}}\mathbf{y}^g}{\sqrt{\kappa_t\kappa_r}}.$$

Following that, the estimated values of $e^{j\phi_0}$ and $e^{j\phi_1}$ are obtained as

$$e^{j\hat{\phi}_0} = \frac{c_{11}\sum_{g=1}^{G}\left(\mathbf{w}_0^g\right)^{\mathrm{H}}\mathbf{y}^g - c_{01}\sum_{g=1}^{G}\left(\mathbf{w}_1^g\right)^{\mathrm{H}}\mathbf{y}^g}{\sqrt{\kappa_t\kappa_r}\rho_0[c_{00}c_{11}-c_{01}c_{10}]} = \frac{C^{(0)}}{\sqrt{\kappa_t\kappa_r}\rho_0}, \tag{35}$$

$$e^{j\hat{\phi}_1} = \frac{c_{00}\sum_{g=1}^{G}\left(\mathbf{w}_1^g\right)^{\mathrm{H}}\mathbf{y}^g - c_{10}\sum_{g=1}^{G}\left(\mathbf{w}_0^g\right)^{\mathrm{H}}\mathbf{y}^g}{\sqrt{\kappa_t\kappa_r}\rho_1[c_{00}c_{11}-c_{01}c_{10}]} = \frac{C^{(1)}}{\sqrt{\kappa_t\kappa_r}\rho_1}, \tag{36}$$

where

$$c_{ij} = \sum_{g=1}^{G}\left(\mathbf{w}_i^g\right)^{\mathrm{H}}\mathbf{w}_j^g,\ i,j=0,1.$$

Next, after substituting the values of $e^{j\hat{\phi}_0}$ and $e^{j\hat{\phi}_1}$ into (22), the log-likelihood function of $\mathbf{y}$ can be given as

$$\begin{aligned} &L(\tau_0,\theta_0,\psi_0,\rho_0,\tau_1,\theta_1,\psi_1,\rho_1) \\ &= -\frac{NG}{2}\ln\left(2\pi\left(KP\left(\rho_0^2+M_{\mathrm{R}}^2\rho_{\mathrm{r}}^2\rho_1^2\right)+\sigma^2\right)\right) \\ &\quad -\frac{\sum_{g=1}^{G}||\mathbf{y}^g - C^{(0)}\mathbf{w}_0^g - C^{(1)}\mathbf{w}_1^g||^2}{2\left(KP\left(\rho_0^2+M_{\mathrm{R}}^2\rho_{\mathrm{r}}^2\rho_1^2\right)+\sigma^2\right)}, \end{aligned} \tag{37}$$

and then the estimated values of ρ_0 and ρ_1 are calculated from

$$\begin{aligned} &\frac{\partial L(\tau_0,\theta_0,\psi_0,\rho_0,\tau_1,\theta_1,\psi_1,\rho_1)}{\partial\rho_0} \\ &= \frac{-NGKP\rho_0}{\left(KP\left(\rho_0^2+M_{\mathrm{R}}^2\rho_{\mathrm{r}}^2\rho_1^2\right)+\sigma^2\right)} \\ &\quad + \frac{KP\rho_0\sum_{g=1}^{G}||\mathbf{y}^g - C^{(0)}\mathbf{w}_0^g - C^{(1)}\mathbf{w}_1^g||^2}{\left(KP\left(\rho_0^2+M_{\mathrm{R}}^2\rho_{\mathrm{r}}^2\rho_1^2\right)+\sigma^2\right)^2} = 0, \\ &\frac{\partial L(\tau_0,\theta_0,\psi_0,\rho_0,\tau_1,\theta_1,\psi_1,\rho_1)}{\partial\rho_1} \\ &= \frac{-NGKPM_{\mathrm{R}}^2\rho_{\mathrm{r}}^2\rho_1}{\left(KP\left(\rho_0^2+M_{\mathrm{R}}^2\rho_{\mathrm{r}}^2\rho_1^2\right)+\sigma^2\right)} \\ &\quad + \frac{KPM_{\mathrm{R}}^2\rho_{\mathrm{r}}^2\rho_1\sum_{g=1}^{G}||\mathbf{y}^g - C^{(0)}\mathbf{w}_0^g - C^{(1)}\mathbf{w}_1^g||^2}{\left(KP\left(\rho_0^2+M_{\mathrm{R}}^2\rho_{\mathrm{r}}^2\rho_1^2\right)+\sigma^2\right)^2} = 0, \end{aligned}$$

which leads to

$$\hat{\rho}_0^2 + M_{\mathrm{R}}^2\rho_{\mathrm{r}}^2\hat{\rho}_1^2 = \frac{\left(\sum_{g=1}^{G}||\mathbf{y}^g - C^{(0)}\mathbf{w}_0^g - C^{(1)}\mathbf{w}_1^g||^2\right) - NG\sigma^2}{NGKP}. \tag{38}$$

Now, with the substitution of $C^{(0)}$ from (35), $C^{(1)}$ from (36) and (38) into (37), the log-likelihood function of $\mathbf{y}$ can be rewritten in terms of τ_0, θ_0, ψ_0,τ_1, θ_1 and ψ_1 as (24).

APPENDIX B
KALMAN FILTER

Referring to [41, Section 13-F] to compare (25) and (26) with the standard form of the Kalman filter for the nonstationary signal, the KFT recursion can be written as the following

$$\hat{\mathbf{p}}_{\mathrm{m}}^{(\mathrm{T})}(t|t-1) \in \mathbb{R}^{3\times1} = \hat{\mathbf{p}}_{\mathrm{m}}^{(\mathrm{T})}(t-1|t-1), \tag{39a}$$

$$\mathbf{N}(t|t-1) \in \mathbb{R}^{3\times3} = \mathbf{N}(t-1|t-1) + \mathbf{Q}, \tag{39b}$$

$$\mathbf{K}(t) \in \mathbb{R}^{3\times3} = \mathbf{N}(t|t-1)(\mathbf{C}(t) + \mathbf{N}(t|t-1))^{-1}, \tag{39c}$$

$$\hat{\mathbf{p}}_{\mathrm{m}}^{(\mathrm{T})}(t|t) \in \mathbb{R}^{3\times1} = \hat{\mathbf{p}}_{\mathrm{m}}^{(\mathrm{T})}(t|t-1) + \mathbf{K}(t)\left(\hat{\mathbf{p}}_{\mathrm{m}}(t) - \hat{\mathbf{p}}_{\mathrm{m}}^{(\mathrm{T})}(t|t-1)\right), \tag{39c}$$

$$\mathbf{N}(t|t) \in \mathbb{R}^{3\times3} = (\mathbf{I}_3 - \mathbf{K}(t))\mathbf{N}(t|t-1), \tag{39d}$$

where $\hat{\mathbf{p}}_{\mathrm{m}}(t)$ is the output from the joint localization-synchronization process obtained according to (24) for the t^{th} position, and $\hat{\mathbf{p}}_{\mathrm{m}}^{(\mathrm{T})}(t|t')$ is the output from the tracker for the t^{th} position, where the current t^{th} tracker output depends on the information from the initial location to the $(t')^{\mathrm{th}}$ location.

Taking a closer looker, (39a) represents the prediction step formulated based on the transition model in (26), while (39b) calculates the minimum prediction MSE matrix $\mathbf{N}$. Moreover, (39c) determines the Kalman gain matrix $\mathbf{K}$ based on matrix $\mathbf{C}$ representing the errors in the estimated positions. Concerning the $\mathbf{C}$ matrix, this work determines its entities according to the CRB of the joint localization-synchronization process derived in the next section and also based on the MC method.

After that, the correction step in (39c) produces the current position $\hat{\mathbf{p}}_{\mathrm{m}}^{(\mathrm{T})}(t|t)$ by correcting the prediction $\hat{\mathbf{p}}_{\mathrm{m}}^{(\mathrm{T})}(t|t-1)$ in (39a) based on the current data $\hat{\mathbf{p}}_{\mathrm{m}}(t)$ from the joint localization-synchronization process. Needless to mention here that the collection of the results of (39c) from the initial output to the t^{th} output constructs the track of the mobile terminal from its initial location to the t^{th} location. Finally, the minimum MSE matrix is given according to (39d).

APPENDIX C
FIM (J_β) ELEMENTS

Let's define the following terms:

$$\begin{aligned} &\overline{\mathbf{F}^g}[n] = \sqrt{\kappa_t}\sqrt{\kappa_r}\mathbf{F}^g[n]\mathbf{z}^g[n], \\ &\frac{\partial\mathbf{k}(\theta_i,\psi_i)}{\partial\theta_i} = [-\sin\psi_i\sin\theta_i, \sin\psi_i\cos\theta_i, 0]^{\mathrm{T}}, \\ &\frac{\partial\mathbf{k}(\theta_i,\psi_i)}{\partial\psi_i} = [\cos\psi_i\cos\theta_i, \cos\psi_i\sin\theta_i, -\sin\psi_i]^{\mathrm{T}}, \\ &\mathbf{B}_{\theta_0} \in \mathbb{R}^{M_{\mathrm{B}}\times M_{\mathrm{B}}} \\ &= \mathrm{diag}\left[\left[\frac{\partial\mathbf{k}(\theta_0,\psi_0)}{\partial\theta_0}\right]^{\mathrm{T}}u_1,\ldots,\left[\frac{\partial\mathbf{k}(\theta_0,\psi_0)}{\partial\theta_0}\right]^{\mathrm{T}}u_{M_{\mathrm{B}}}\right], \\ &\mathbf{B}_{\psi_0} \in \mathbb{R}^{M_{\mathrm{B}}\times M_{\mathrm{B}}} \\ &= \mathrm{diag}\left[\left[\frac{\partial\mathbf{k}(\theta_0,\psi_0)}{\partial\psi_0}\right]^{\mathrm{T}}u_1,\ldots,\left[\frac{\partial\mathbf{k}(\theta_0,\psi_0)}{\partial\psi_0}\right]^{\mathrm{T}}u_{M_{\mathrm{B}}}\right], \\ &\mathbf{B}_{\theta_1} \in \mathbb{R}^{M_{\mathrm{R}}\times M_{\mathrm{R}}} \end{aligned}$$

$$= \text{diag}\left[\left[\frac{\partial \mathbf{k}(\theta_1,\psi_1)}{\partial \theta_1}\right]^{\mathrm{T}} u_1, \ldots, \left[\frac{\partial \mathbf{k}(\theta_1,\psi_1)}{\partial \theta_1}\right]^{\mathrm{T}} u_{M_{\mathrm{R}}}\right],$$

$$\mathbf{B}_{\psi_1} \in \mathbb{R}^{M_{\mathrm{R}}\times M_{\mathrm{R}}}$$

$$= \text{diag}\left[\left[\frac{\partial \mathbf{k}(\theta_1,\psi_1)}{\partial \psi_1}\right]^{\mathrm{T}} u_1, \ldots, \left[\frac{\partial \mathbf{k}(\theta_1,\psi_1)}{\partial \psi_1}\right]^{\mathrm{T}} u_{M_{\mathrm{R}}}\right].$$

Next, by calculating the derivations of the following terms $\varphi^g[n]$ and C_y with respect to β as follows: Next, the derivations of $\varphi^g[n]$ with respect to vector β are

$$\begin{aligned}
\frac{\partial \varphi^g[n]}{\partial \tau_0} &= \frac{-j2\pi n}{NT}\rho_0 \exp\Big(j(\phi_0 - 2\pi n\frac{\tau_0}{NT})\Big) \\
&\quad \times \alpha(\theta_0,\psi_0,M_{\mathrm{B}})^{\mathrm{T}}\,\overline{\mathbf{F}^g}[n], \\
\frac{\partial \varphi^g[n]}{\partial \theta_0} &= j\frac{2\pi}{\lambda_c}\rho_0 \exp\big(j(\phi_0 - 2\pi n\tfrac{\tau_0}{NT})\big) \\
&\quad \times \alpha(\theta_0,\psi_0,M_{\mathrm{B}})^{\mathrm{T}}\mathbf{B}_{\theta_0}\overline{\mathbf{F}^g}[n], \\
\frac{\partial \varphi^g[n]}{\partial \psi_0} &= j\frac{2\pi}{\lambda_c}\rho_0 \exp\big(j(\phi_0 - 2\pi n\tfrac{\tau_0}{NT})\big) \\
&\quad \times \alpha(\theta_0,\psi_0,M_{\mathrm{B}})^{\mathrm{T}}\mathbf{B}_{\psi_0}\overline{\mathbf{F}^g}[n], \\
\frac{\partial \varphi^g[n]}{\partial \rho_0} &= e^{j\phi_0}e^{-j2\pi n\frac{\tau_0}{NT}}\alpha(\theta_0,\psi_0,M_{\mathrm{B}})^{\mathrm{T}}\,\overline{\mathbf{F}^g}[n]. \\
\frac{\partial \varphi^g[n]}{\partial \phi_0} &= j\rho_0 e^{j\phi_0}e^{-j2\pi n\frac{\tau_0}{NT}}\alpha(\theta_0,\psi_0,M_{\mathrm{B}})^{\mathrm{T}}\,\overline{\mathbf{F}^g}[n], \\
\frac{\partial \varphi^g[n]}{\partial \tau_1} &= \frac{-j2\pi n}{NT}\rho_1 e^{j\phi_1}e^{-j2\pi n\frac{\tau_1}{NT}} \\
&\quad \times \alpha(\theta_1,\psi_1,M_{\mathrm{R}})^{\mathrm{T}}\Omega^g(\mathbf{H}_{\mathrm{r}}[n])^{\mathrm{T}}\overline{\mathbf{F}^g}[n], \\
\frac{\partial \varphi^g[n]}{\partial \theta_1} &= j\frac{2\pi}{\lambda_c}\rho_1 \exp\big(j(\phi_1 - 2\pi n\tfrac{\tau_1}{NT})\big) \\
&\quad \times \alpha(\theta_1,\psi_1,M_{\mathrm{R}})^{\mathrm{T}}\mathbf{B}_{\theta_1}\Omega^g(\mathbf{H}_{\mathrm{r}}[n])^{\mathrm{T}}\,\overline{\mathbf{F}^g}[n], \\
\frac{\partial \varphi^g[n]}{\partial \psi_1} &= j\frac{2\pi}{\lambda_c}\rho_1 \exp\big(j(\phi_1 - 2\pi n\tfrac{\tau_1}{NT})\big) \\
&\quad \times \alpha(\theta_1,\psi_1,M_{\mathrm{R}})^{\mathrm{T}}\mathbf{B}_{\psi_1}\Omega^g(\mathbf{H}_{\mathrm{r}}[n])^{\mathrm{T}}\,\overline{\mathbf{F}^g}[n], \\
\frac{\partial \varphi^g[n]}{\partial \rho_1} &= \exp\big(j(\phi_1 - 2\pi n\tfrac{\tau_1}{NT})\big) \\
&\quad \times \alpha(\theta_1,\psi_1,M_{\mathrm{R}})^{\mathrm{T}}\Omega^g(\mathbf{H}_{\mathrm{r}}[n])^{\mathrm{T}}\overline{\mathbf{F}^g}[n], \\
\frac{\partial \varphi^g[n]}{\partial \phi_1} &= j\rho_1 \exp\big(j(\phi_1 - 2\pi n\tfrac{\tau_1}{NT})\big) \\
&\quad \times \alpha(\theta_1,\psi_1,M_{\mathrm{R}})^{\mathrm{T}}\Omega^g(\mathbf{H}_{\mathrm{r}}[n])^{\mathrm{T}}\,\overline{\mathbf{F}^g}[n],
\end{aligned}$$

while the derivatives of the noise variance C_y with respect to the same vector can be calculated as

$$\begin{aligned}
\frac{\partial C_y}{\partial \rho_0} &= 2P(1-\kappa_t\kappa_r)M_{\mathrm{B}}\rho_0, \\
\frac{\partial C_y}{\partial \rho_1} &= 2P(1-\kappa_t\kappa_r)M_{\mathrm{B}}M_{\mathrm{R}}^2\rho_{\mathrm{r}}^2\rho_1. \\
\frac{\partial C_y}{\partial \tau_0} &= \frac{\partial C_y}{\partial \theta_0} = \frac{\partial C_y}{\partial \psi_0} = \frac{\partial C_y}{\partial \phi_0} = \frac{\partial C_y}{\partial \tau_1} \\
&= \frac{\partial C_y}{\partial \theta_1} = \frac{\partial C_y}{\partial \psi_1} = \frac{\partial C_y}{\partial \phi_1} = 0.
\end{aligned}$$

APPENDIX D
TRANSFORMATION MATRIX (*T*) ELEMENTS

Based on the definition in (30) and depending on the geometric relationships between the elements of the two vectors β and μ, the $\mathbf{T}$ matrix is a zero matrix except for the following elements:

$$\begin{aligned}
&\frac{\partial \tau_0}{\partial \Delta} = \frac{\partial \tau_1}{\partial \Delta} = 1, \quad \frac{\partial \tau_0}{\partial \mathrm{p}_x} = \frac{\mathrm{p}_x}{c\sqrt{\mathrm{p}_x^2+\mathrm{p}_y^2+\mathrm{p}_z^2}}, \\
&\frac{\partial \tau_0}{\partial \mathrm{p}_y} = \frac{\mathrm{p}_y}{c\sqrt{\mathrm{p}_x^2+\mathrm{p}_y^2+\mathrm{p}_z^2}}, \quad \frac{\partial \tau_0}{\partial \mathrm{p}_z} = \frac{\mathrm{p}_z}{c\sqrt{\mathrm{p}_x^2+\mathrm{p}_y^2+\mathrm{p}_z^2}}, \\
&\frac{\partial \theta_0}{\partial \mathrm{p}_x} = \frac{-\mathrm{p}_y}{\mathrm{p}_x^2+\mathrm{p}_y^2}, \quad \frac{\partial \theta_0}{\partial \mathrm{p}_y} = \frac{\mathrm{p}_x}{\mathrm{p}_x^2+\mathrm{p}_y^2}, \\
&\frac{\partial \psi_0}{\partial \mathrm{p}_x} = \frac{|\mathrm{p}_z|\mathrm{p}_x}{\left(\mathrm{p}_x^2+\mathrm{p}_y^2+\mathrm{p}_z^2\right)\sqrt{\mathrm{p}_x^2+\mathrm{p}_y^2}}, \\
&\frac{\partial \psi_0}{\partial \mathrm{p}_y} = \frac{|\mathrm{p}_z|\mathrm{p}_y}{\left(\mathrm{p}_x^2+\mathrm{p}_y^2+\mathrm{p}_z^2\right)\sqrt{\mathrm{p}_x^2+\mathrm{p}_y^2}}, \\
&\frac{\partial \psi_0}{\partial \mathrm{p}_z} = \frac{-\mathrm{p}_z\sqrt{\mathrm{p}_x^2+\mathrm{p}_y^2}}{|\mathrm{p}_z|\left(\mathrm{p}_x^2+\mathrm{p}_y^2+\mathrm{p}_z^2\right)}, \\
&\frac{\partial \tau_1}{\partial \mathrm{p}_x} = \frac{(\mathrm{p}_x-\mathrm{r}_x)}{c\sqrt{(\mathrm{p}_x-\mathrm{r}_x)^2+(\mathrm{p}_y-\mathrm{r}_y)^2+(\mathrm{p}_z-\mathrm{r}_z)^2}}, \\
&\frac{\partial \tau_1}{\partial \mathrm{p}_y} = \frac{(\mathrm{p}_y-\mathrm{r}_y)}{c\sqrt{(\mathrm{p}_x-\mathrm{r}_x)^2+(\mathrm{p}_y-\mathrm{r}_y)^2+(\mathrm{p}_z-\mathrm{r}_z)^2}}, \\
&\frac{\partial \tau_1}{\partial \mathrm{p}_z} = \frac{(\mathrm{p}_z-\mathrm{r}_z)}{c\sqrt{(\mathrm{p}_x-\mathrm{r}_x)^2+(\mathrm{p}_y-\mathrm{r}_y)^2+(\mathrm{p}_z-\mathrm{r}_z)^2}}, \\
&\frac{\partial \theta_1}{\partial \mathrm{p}_x} = \frac{-\frac{\mathrm{p}_y-\mathrm{r}_y}{(\mathrm{p}_x-\mathrm{r}_x)^2}}{1+\left(\frac{\mathrm{p}_y-\mathrm{r}_y}{\mathrm{p}_x-\mathrm{r}_x}\right)^2}, \quad \frac{\partial \theta_1}{\partial \mathrm{p}_y} = \frac{1/(\mathrm{p}_x-\mathrm{r}_x)}{1+\left(\frac{\mathrm{p}_y-\mathrm{r}_y}{\mathrm{p}_x-\mathrm{r}_x}\right)^2}, \\
&\frac{\partial \psi_1}{\partial \mathrm{p}_x} = \frac{|\mathrm{p}_z-\mathrm{r}_z|(\mathrm{p}_x-\mathrm{r}_x)/\sqrt{(\mathrm{p}_x-\mathrm{r}_x)^2+(\mathrm{p}_y-\mathrm{r}_y)^2}}{(\mathrm{p}_x-\mathrm{r}_x)^2+(\mathrm{p}_y-\mathrm{r}_y)^2+(\mathrm{p}_z-\mathrm{r}_z)^2}, \\
&\frac{\partial \psi_1}{\partial \mathrm{p}_y} = \frac{|\mathrm{p}_z-\mathrm{r}_z|(\mathrm{p}_y-\mathrm{r}_y)/\sqrt{(\mathrm{p}_x-\mathrm{r}_x)^2+(\mathrm{p}_y-\mathrm{r}_y)^2}}{(\mathrm{p}_x-\mathrm{r}_x)^2+(\mathrm{p}_y-\mathrm{r}_y)^2+(\mathrm{p}_z-\mathrm{r}_z)^2}, \\
&\frac{\partial \psi_1}{\partial \mathrm{p}_z} = \frac{-(\mathrm{p}_z-\mathrm{r}_z)\sqrt{(\mathrm{p}_x-\mathrm{r}_x)^2+(\mathrm{p}_y-\mathrm{r}_y)^2}/|\mathrm{p}_z-\mathrm{r}_z|}{(\mathrm{p}_x-\mathrm{r}_x)^2+(\mathrm{p}_y-\mathrm{r}_y)^2+(\mathrm{p}_z-\mathrm{r}_z)^2}.
\end{aligned}$$

REFERENCES

[1] Z. Abu-Shaban, X. Zhou, T. D. Abhayapala, G. Seco-Granados, and H. Wymeersch, "Error bounds for uplink and downlink 3D localization in 5G millimeter wave systems," *IEEE Trans. Wireless Commun.*, vol. 17, no. 8, pp. 4939–4954, Aug. 2018.

[2] A. Shahmansoori, G. E. Garcia, G. Destino, G. Seco-Granados, and H. Wymeersch, "Position and orientation estimation through millimeter-wave MIMO in 5G systems," *IEEE Trans. Wireless Commun.*, vol. 17, no. 3, pp. 1822–1835, Mar. 2018.

[3] F. Ghaseminajm, Z. Abu-Shaban, S. Ikki, H. Wymeersch, and C. R. Benson, "Localization error bounds for 5G mmWave systems under I/Q imbalance," *IEEE Trans. Veh. Technol.*, vol. 69, no. 7, pp. 7971–7975, Jul. 2020.

[4] Z. Marzi, D. Ramasamy, and U. Madhow, "Compressive channel estimation and tracking for large arrays in mm-wave picocells," *IEEE J. Sel. Topics Signal Process.*, vol. 10, no. 3, pp. 514–527, Apr. 2016.

[5] B. Zhou, A. Liu, and V. Lau, "Successive localization and beamforming in 5G mmWave MIMO communication systems," *IEEE Trans. Signal Process.*, vol. 67, no. 6, pp. 1620–1635, Mar. 2019.

[6] K. Witrisal et al., "High-accuracy localization for assisted living: 5G systems will turn multipath channels from foe to friend," *IEEE Signal Process. Mag.*, vol. 33, no. 2, pp. 59–70, Mar. 2016.

[7] C. Zhang, D. Guo, and P. Fan, "Tracking angles of departure and arrival in a mobile millimeter wave channel," in *Proc. IEEE Int. Conf. Commun. (ICC)*, Kuala Lumpur, Malaysia, 2016, pp. 1–6.

[8] K. Keykhosravi, M. F. Keskin, G. Seco-Granados, P. Popovski, and H. Wymeersch, "RIS-enabled SISO Localization under user mobility and spatial-wideband effects," *IEEE J. Sel. Topics Signal Process.*, vol. 16, no. 5, pp. 1125–1140, Aug. 2022.

[9] T. Ma, Y. Xiao, X. Lei, L. Zhang, Y. Niu, and G. K. Karagiannidis, "Reconfigurable intelligent surface-assisted localization: Technologies, challenges, and the road ahead," *IEEE Open J. Commun. Soc.*, vol. 4, pp. 1430–1451, 2023.

[10] A. Elzanaty, A. Guerra, F. Guidi, and M.-S. Alouini, "Reconfigurable intelligent surfaces for Localization: Position and orientation error bounds," *IEEE Trans. Signal Process.*, vol. 69, pp. 5386–5402, Aug. 2021, doi: 10.1109/TSP.2021.3101644.

[11] J. He, H. Wymeersch, L. Kong, O. Silven, and M. Juntti, "Large intelligent surface for positioning in millimeter wave MIMO systems," in *Proc. IEEE 91st Veh. Technol. Conf. (VTC)*, Antwerp, Belgium, 2020, pp. 1–5.

[12] A. Fascista, M. Keskin, A. Coluccia, H. Wymeersch, and G. Seco-Granados, "RIS-aided joint Localization and Synchronization with a single-antenna receiver: Beamforming design and low-complexity estimation," *IEEE J. Sel. Topics Signal Process.*, vol. 16, no. 5, pp. 1141–1156, Aug. 2022.

[13] A. Fascista, A. Coluccia, H. Wymeersch, and G. Seco-Granados, "RIS-aided joint localization and Synchronization with a single-antenna MmWave receiver," in *Proc. IEEE Int. Conf. Acoust., Speech Signal Process. (ICASSP)*, Toronto, ON, Canada, 2021, pp. 4455–4459.

[14] D.-R. Emenonye, H. S. Dhillon, and R. M. Buehrer, "Fundamentals of RIS-aided localization in the far-field," *IEEE Trans. Wireless Commun.*, early access, Aug. 29, 2023, doi: 10.1109/TWC.2023.3307818.

[15] D.-R. Emenonye, H. S. Dhillon, and R. Michael Buehrer, "RIS-aided Localization under position and orientation offsets in the near and far field," *IEEE Trans. Wireless Commun.*, vol. 22, no. 12, pp. 9327–9345, Dec. 2023.

[16] H. Li, Y. Zhang, J. Xi, and W. Guo, "3D beam tracking method based on reconfigurable intelligent surface assistant for blocking channel," in *Proc. 36th Youth Acad. Annu. Conf. Chin. Assoc. Autom. (YAC)*, Nanchang, China, 2021, pp. 684–689.

[17] J. Yuan, G. C. Alexandropoulos, E. Kofidis, T. L. Jensen, and E. D. Carvalho, "Channel tracking for RIS-enabled multi-user SIMO systems in time-varying wireless channels," in *Proc. IEEE Int. Conf. Commun. Workshops*, Seoul, South Korea, 2022, pp. 145–150.

[18] X. Wang et al., "Codebook-based beam tracking for RIS assisted mobile MmWave networks," in *Proc. 13th Int. Symp. Antennas, Propag. EM Theory (ISAPE)*, Zhuhai, China, 2021, pp. 1–3.

[19] B. Teng, X. Yuan, R. Wang, and S. Jin, "Bayesian user localization and tracking for reconfigurable intelligent surface aided MIMO systems," *IEEE J. Sel. Topics Signal Process.*, vol. 16, no. 5, pp. 1040–1054, Aug. 2022.

[20] Y. Chen, Y. Wang, X. Guo, Z. Han, and P. Zhang, "Location tracking for reconfigurable intelligent surfaces aided vehicle platoons: Diverse sparsities inspired approaches," *IEEE J. Sel. Areas Commun.*, vol. 41, no. 8, pp. 2476–2496, Aug. 2023.

[21] E. Björnson, J. Hoydis, and L. Sanguinetti, *Massive MIMO Networks: Spectral, Energy, and Hardware Efficiency*, vol. 11. Delft, The Netherlands: Now Publ. Inc., 2017. [Online]. Available: http://www.nowpublishers.com

[22] B. Cenikliogluu, I. Develi, A. E. Canbilen, and M. Lafci, "Analysis of average bit error rate for OFDM-IM systems with hardware impairments over Nakagami-m and Weibull fading channels," in *Proc. Int. Conf. Comput., Commun. Secur. Intell. Syst.*, 2022, pp. 1–6.

[23] H. Mehrpouyan, M. Matthaiou, R. Wang, G. Karagiannidis, and Y. Hua, "Hybrid millimeter-wave systems: A novel paradigm for HetNets," *IEEE Commun. Mag.*, vol. 53, no. 1, pp. 216–221, Jan. 2015.

[24] F. Ghaseminajm, E. Saleh, M. M. Alsmadi, and S. Ikki, "Localization error bounds for 5G mmWave systems under hardware impairments," in *Proc. IEEE 32nd Annu. Int. Symp. Pers., Indoor, Mobile Radio Commun.*, Helsinki, Finland, 2021, pp. 1228–1233.

[25] D. A. Tubail, B. Cenikliogluu, A. E. Canbilen, I. Develi, and S. Ikki, "Error bounds for 3D localization and maximum likelihood estimation of *mm*-wave MISO OFDM systems in the presence of hardware impairments," *IEEE Commun. Lett.*, vol. 26, no. 9, pp. 2042–2046, Sep. 2022.

[26] F. Ghaseminajm, M. Alsmadi, D. Tubail, and S. S. Ikki, "RIS-aided mobile localization error bounds under hardware impairments," *IEEE Trans. Commun.*, vol. 70, no. 12, pp. 8331–8341, Aug. 2022.

[27] D. Zhu, J. Choi, Q. Cheng, W. Xiao, and R. W. Heath, "High-resolution angle tracking for mobile wideband millimeter-wave systems with antenna array calibration," *IEEE Trans. Wireless Commun.*, vol. 17, no. 11, pp. 7173–7189, Nov. 2018.

[28] Y. Yang, S. Dang, M. Wen, S. Mumtaz, and M. Guizani, "Bayesian beamforming for mobile millimeter wave channel tracking in the presence of DOA uncertainty," *IEEE Trans. Commun.*, vol. 68, no. 12, pp. 7547–7562, Dec. 2020.

[29] O. S. Faragallah, H. S. El-Sayed, and M. G. El-Mashed, "Estimation and tracking for millimeter wave MIMO systems under phase noise problem," *IEEE Access*, vol. 8, pp. 228009–228023, 2020.

[30] D. Tubail, B. Cenikliogluu, A. E. Canbilen, I. Develi, and S. S. Ikki, "The effect of hardware impairments on the error bounds of localization and maximum likelihood estimation of mm-wave MISO-OFDM systems," *IEEE Trans. Veh. Technol.*, vol. 72, no. 3, pp. 4063–4067, Mar. 2023.

[31] D. A. Tubail and S. Ikki, "Range-direction tracking and Bayesian Cramer-Rao bound analysis in mmwave systems equipped with imperfect transceivers," *IEEE Wireless Commun. Lett.*, vol. 12, no. 10, pp. 1806–1810, Oct. 2023.

[32] F. Ghaseminajm, M. Alsamdi, and S. S. Ikki, "Error bounds for localization in *mm*wave MIMO systems: Effects of hardware impairments considering perfect and imperfect clock synchronization," *IEEE Syst. J.*, vol. 16, no. 4, pp. 6350–6359, Dec. 2022.

[33] B. Cenikliogluu, D. Tubail, A. E. Canbilen, I. Develi, and S. Ikki, "Error analysis of the joint localization and synchronization of RIS-assisted *mm*-wave MISO-OFDM under the effect of hardware impairments," *IEEE Open J. Commun. Soc.*, vol. 3, pp. 2151–2161, 2022.

[34] A. Fascista, A. Coluccia, H. Wymeersch, and G. Seco-Granados, "Millimeter-wave downlink positioning with a single-antenna receiver," *IEEE Trans. Wireless Commun.*, vol. 18, no. 9, pp. 4479–4490, Sep. 2019.

[35] F. Horlin and A. Bourdoux, *Digital Compensation for Analog Front-Ends: A New Approach to Wireless Transceiver Design*. Hoboken, NJ, USA: Wiley, 2008.

[36] T. Schenk, *RF Imperfections in High-Rate Wireless Systems:Impact and Digital Compensation*. Dordrecht, The Netherlands: Springer, 2008.

[37] G. Hueber and R. B. Staszewski, "RF impairment compensation for future radio systems," in *Multi-Mode/Multi-Band RF Transceivers for Wireless Communications: Advanced Techniques, Architectures, and Trends*. Hoboken, NJ, USA: Wiley, 2011, pp. 451–496.

[38] E. Bjornson, J. Hoydis, M. Kountouris, and M. Debbah, "Massive MIMO systems with non-ideal hardware: Energy efficiency, estimation, and capacity limits," *IEEE Trans. Inf. Theory*, vol. 60, no. 11, pp. 7112–7139, Nov. 2014.

[39] A. Alkhateeb and R. W. Heath, "Frequency selective hybrid precoding for limited feedback millimeter wave systems," *IEEE Trans. Commun.*, vol. 64, no. 5, pp. 1801–1818, May 2016.

[40] C. N. Barati et al., "Initial access in millimeter wave cellular systems," *IEEE Trans. Wireless Commun.*, vol. 15, no. 12, pp. 7926–7940, Dec. 2016.

[41] S. M. Kay, *Fundamentals of Statistical Signal Processing: Estimation Theory*, vol. 1. Englewood Cliffs, NJ, USA: Prentice-Hall, 1993.

[42] B. Anderson and J. Moore, "Optimal filtering," in *Prentice-Hall Information and System Sciences Series*, Sebastopol, CA, USA, 1979.

[43] P. Tichavsky, C. H. Muravchik, and A. Nehorai, "Posterior Cramer–Rao bounds for discrete-time nonlinear filtering," *IEEE Trans. Signal Process.*, vol. 46, no. 5, pp. 1386–1396, May 1998.

DEEB ASSAD TUBAIL (Graduate Student Member, IEEE) received the Honors Bachelor's degree in electrical engineering and the Honors Master's degree in telecommunication from the Islamic University of Gaza, Palestine, in 2009 and 2014, respectively, and the Ph.D. degree with the Electrical and Computer Engineering Department, Lakehead University, Canada, in 2023. The research focused on wireless communication, covering areas, such as estimation, localization, tracking, performance analysis, physical-layer security, and massive MIMO. The master's research delved into the microwave domain, specifically in coupled-resonators circuits, and microwave devices. He engaged currently in ongoing research in wireless communication, particularly in OTFS modulation, and machine learning.

MOHAMMED EL-ABSI (Member, IEEE) received the B.E. degree in electrical engineering from the Islamic University of Gaza, Gaza, Palestine, in 2005, the M.S. degree in electrical engineering from the Jordan University of Science and Technology, Irbid, Jordan, in 2008, and the Ph.D. degree (summa cum laude) in electrical engineering from the University of Duisburg-Essen, Duisburg, Germany, in 2015, where he is currently a Senior Researcher with the Digital Signal Processing Institute. He is also a Principal Investigator of the excellent terahertz research for communication, localization, material characterization, medical technology, and environmental monitoring (teraherty.NRW). He is also contributing in 6G research hub for open, efficient, and secure mobile radio systems and the Collaborative Research Center "Mobile Material Characterization and Localization by Electromagnetic Sensing" (MARIE). His research interests include communications and signal processing. He was a recipient of a Mercator Fellow with the Collaborative Research Center MARIE, from 2017 to 2018, and the German Academic Exchange Service Fellowship, from 2006 to 2011.

SALAMA IKKI (Senior Member, IEEE) is currently a Professor and the Research Chair of wireless communications with Lakehead University, Thunder Bay, ON, Canada. In 2022, he was a Visiting Research Professor (Nokia Scholarship) with Aalto University, Helsinki, Finland. He is an Author of more than 100 journals and conference papers and has more than 5500 citations and an H-index of 36. His research group has made substantial contributions to 4G and 5G wireless technologies. His group's current research interests include massive MIMO, cell-free massive MIMO, visible light communications, and wireless sensor networks. He was a recipient of several awards for research, teaching, and services.

THOMAS KAISER (Senior Member, IEEE) received the Diploma degree in electrical engineering from Ruhr-University Bochum, Bochum, Germany, in 1991 and the Ph.D. (with distinction) and German Habilitation degrees in electrical engineering from Gerhard Mercator University, Duisburg, Germany in 1995 and 2000, respectively. From 1995 to 1996, he spent a research leave with the University of Southern California, Los Angeles, which was grant-aided by the German Academic Exchange Service. From April 2000 to March 2001, he was the Head of the Department of Communication Systems, Gerhard Mercator University, and from April 2001 to March 2002, he was the Head of the Department of Wireless Chips and Systems, Fraunhofer Institute of Microelectronic Circuits and Systems, Duisburg. From April 2002 to July 2006, he was a Co-Leader of the Smart Antenna Research Team, University of Duisburg-Essen, Duisburg. In summer of 2005, he joined the Smart Antenna Research Group, Stanford University, Stanford, CA, and in winter of 2007, he joined the Department of Electrical Engineering, Princeton University, Princeton, NJ, USA, both as a Visiting Professor. From 2006 to 2011, he headed with the Institute of Communication Technology, Leibniz University of Hannover, Germany. He Heads with the Institute of Digital Signal Processing, University of Duisburg-Essen and the Founder and CEO of ID4us GmbH, an RFID Centric Company. He is the author and coauthor of more than 350 papers in international journals and conference proceedings and two books entitled *Ultra Wideband Systems With MIMO* (Wiley, 2010) and *Digital Signal Processing for RFID* (Wiley, 2015) and he is the Speaker of the Collaborative Research Center "Mobile Material Characterization and Localization by Electromagnetic Sensing." He also the Co-Founded of several Hightech-Startups. He was the founding Editor-in-Chief of the e-letter of the IEEE SIGNAL PROCESSING SOCIETY and the General Chair of the IEEE International Conference on UltraWideBand in 2008, the International Conference on Cognitive Radio Oriented Wireless Networks and Communications in 2009, the IEEE Workshop on Cellular Cognitive Systems in 2014, and the IEEE Conference on Mobile and Miniaturized THz Systems from 2018 to 2025.